Submesoscale Mixing on Initial Dilution of Radionuclides Released From the Fukushima Daiichi Nuclear Power Plant

Kamidaira, Yuki
Uchiyama, Yusuke
Kawamura, Hideyuki
Kobayashi, Takuya
Furuno, Akiko

(Citation)
Journal of Geophysical Research: Oceans,123(4):2808-2828

(Issue Date)
2018-04

(Resource Type)
journal article

(Version)
Version of Record

(URL)
https://hdl.handle.net/20.500.14094/90006807

Journal of Geophysical Research: Oceans

RESEARCH ARTICLE
10.1002/2017JC013359

Submesoscale Mixing on Initial Dilution of Radionuclides Released From the Fukushima Daiichi Nuclear Power Plant

Yuki Kamidaira[1,2], Yusuke Uchiyama[2,3], Hideyuki Kawamura[1], Takuya Kobayashi[1], and Akiko Furuno[1]

[1]Nuclear Science and Engineering Center, Japan Atomic Energy Agency, Tokai, Japan, [2]Department of Civil Engineering, Kobe University, Kobe, Japan, [3]Coastal and Estuarine Environment Department, Port and Airport Research Institute, Yokosuka, Japan

Key Points:
- Oceanic dispersal of dissolved radionuclides is investigated using a high-resolution, coupled circulation-offline Eulerian transport model
- Submesoscale eddy-induced ageostrophic secondary circulations (ASCs) notably promoted vertical mixing shortly after the nuclear accident
- ASCs occur primarily because of shear instability, with baroclinic instability under late winter conditions when the initial dilution occurred

Supporting Information:
- Data Set S1

Correspondence to:
Y. Kamidaira,
kamidaira.yuki@jaea.go.jp

Citation:
Kamidaira, Y., Uchiyama, Y., Kawamura, H., Kobayashi, T., & Furuno, A. (2018). Submesoscale mixing on initial dilution of radionuclides released from the Fukushima Daiichi Nuclear Power Plant. *Journal of Geophysical Research: Oceans*, *123*, 2808–2828. https://doi.org/10.1002/2017JC013359

Received 15 AUG 2017
Accepted 16 MAR 2018
Accepted article online 26 MAR 2018
Published online 24 APR 2018

Abstract This study developed a submesoscale eddy-resolving oceanic dispersal modeling system comprising a double-nested oceanic downscaling model and an offline oceanic radionuclide dispersion model. This was used to investigate the influences of submesoscale coherent structures (SCSs) and associated ageostrophic secondary circulations (ASCs) on the three-dimensional (3-D) dispersal of dissolved cesium-137 (^{137}Cs) released from the Fukushima Daiichi Nuclear Power Plant (FNPP1). Extensive model-data comparison demonstrated that the innermost high-resolution model, with a lateral grid resolution of 1 km, could successfully reproduce transient mesoscale oceanic structures, the Kuroshio path and stratification, and spatiotemporal variations of ^{137}Cs concentrations. Using an accompanying mesoscale eddy-resolving model (grid resolution: 10 km) as a guide, we showed that submesoscale dynamics are important for improved representation of both the eddy field and the resultant 3-D dispersal of ^{137}Cs, with the temporal variability of surface ^{137}Cs near the FNPP1 being equivalent to that in the coarse-resolution model. According to energy conversion and spectral analyses, SCSs and ASCs occur most intensively on the submesoscale, primarily because of shear instability. However, baroclinic instability serves as a secondary mechanism. SCSs have prominent seasonality, reflected by intensification in the colder months, which is when the FNPP1 accident occurred. Analysis of the vertical flux of ^{137}Cs was performed by decomposition of the variables into eddy, mesoscale, and submesoscale components using frequency and wave number filters. It revealed that 42.7% of the FNPP1-derived ^{137}Cs was transported downward below the mixed layer by eddies with the major contribution being from ASCs induced by submesoscale eddies.

1. Introduction

At 14:46 JST on 11 March 2011, a magnitude 9.0 earthquake occurred off the Pacific coast of Tohoku, Japan, generating catastrophic tsunamis that struck the Tohoku coast (Mori et al., 2011). Inundation and runup height of the tsunamis reached 15 m at the Fukushima Daiichi Nuclear Power Plant (FNPP1). Subsequently, the cooling system for the reactors was severely damaged, which led to three nuclear meltdowns and hydrogen-air explosions. Consequently, substantial amounts of radioactive substances were released accidentally from the FNPP1 to both the atmosphere and the ocean (Nuclear Emergency Response Headquarters, Government of Japan, 2011).

Several modeling studies on source term estimation, in relation to the accidental release, have been conducted because the acquisition of suitable measurements was extremely difficult to accomplish shortly after the accident. Among others, the Japan Atomic Energy Agency (JAEA) estimated the temporal variations of leaked radionuclide doses during the accident using atmospheric and oceanic transport, dispersion, and deposition models. Kawamura et al. (2011) reported that the total amount of oceanic direct release of cesium-137 (^{137}Cs; half-life = 30.17 years, e.g., National Institute of Standards and Technology, https://www.nist.gov/pml/radionuclide-half-life-measurements-data) from 21 March to 30 April 2011, was estimated to be 4 PBq, which agrees well with the model-based estimate by Tsumune et al. (2012). Katata et al. (2015) estimated the atmospheric release of ^{137}Cs from the FNPP1 to be 14.5 PBq from 12 March to 1 May 2011, which is consistent with estimates reported in several other studies (e.g., Aoyama et al., 2016a; Inomata et al., 2016; Tsubono et al., 2016).

Model assessments have also been undertaken to investigate the oceanic dispersal of the radionuclides that leaked from the FNPP1 on and around the continental shelf off Fukushima, with primary focus on the surface transport of dissolved ^{137}Cs. For example, Miyazawa et al. (2012) conducted a numerical hindcast for dissolved ^{137}Cs, released directly from the FNPP1, using an Eulerian passive tracer transport model coupled with a regional circulation model (horizontal resolution: 1/36°, i.e., ∼3 km) based on the hydrodynamic kernel of the Japan Coastal Ocean Predictability Experiments (JCOPE2) system (Miyazawa et al., 2009). They performed a series of experiments to determine the sensitivity of oceanic ^{137}Cs dispersal to surface winds, tides, and river discharges, and they highlighted that the role played by wind facilitates the meridional extension of the distribution of surface ^{137}Cs on the shelf. Estournel et al. (2012) modeled oceanic ^{137}Cs dispersal by considering both direct release and atmospheric deposition using the SYMPHONIE model (Marsaleix et al., 2009, 2012) with variable horizontal grid sizes that increased linearly from 600 m to 5.5 km with distance from the FNPP1. They identified that in addition to the importance of wind, riverine freshwater discharges promoted the offshore transport of ^{137}Cs via surface-concentrated buoyant plumes. Masumoto et al. (2012) conducted an intermodel comparison of oceanic ^{137}Cs dispersal using five different regional oceanic models (including the preceding two models) at horizontal resolutions ranging from 600 m to 3.0 km. The five models were found to show overall qualitative similarities, despite substantial differences in the detail of their processes. Modeled surface ^{137}Cs dispersal depends considerably on the lateral grid resolution of the model, where coarser resolution (e.g., grid spacing $\gg$ 1 km) models tend to overestimate the cross-shelf transport. In contrast, finer-resolution models are more capable of reproducing the prevailing coastally trapped alongshelf transport that acts to retard immediate offshore transport and subsequent dilution via the synoptic Kuroshio-Oyashio current system. In summary, previous studies have identified four key mechanisms that could have determined the initial oceanic dispersal of the FNPP1-derived dissolved ^{137}Cs shortly after the accident occurred: (1) wind-driven, coastally trapped alongshelf currents; (2) buoyancy inputs from adjacent rivers; (3) a mesoscale clockwise lateral circulation that developed southwest of the FNPP1 in April 2011 associated with the migration of a warm-core eddy pinched off from the Kuroshio Extension Jet, which interacted with (1); and (4) the Kuroshio-Oyashio system, which was responsible for subsequent offshore dispersal and dilution.

Compared with surface processes, much less attention has been paid to the subsurface three-dimensional (3-D) transport. The numerical hindcast by Tsumune et al. (2012, 2013) could be regarded as one of the most successful high-resolution (1 km lateral resolution) modeling studies because it has been used as a benchmark for other models (e.g., Estournel et al., 2012; Kawamura et al., 2014). Its results are generally found consistent with in situ ^{137}Cs measurements, temporally, spatially, and in terms of vertical distributions, despite the deficiencies of their modeling strategy, e.g., the large nesting grid-size ratio (viz., the parent 10 km resolution is downscaled directly to the child 1 km resolution), lack of river inputs, and the neglect of topography deeper than 1,000 m. In contrast, the mesoscale eddy-resolving oceanic cesium-134 (^{134}Cs; half-life = 2.07 years) and ^{137}Cs dispersal modeling (horizontal grid resolution: 1/10°) conducted by Kawamura et al. (2014) underestimated subsurface cesium concentrations, particularly in intermediate (depth: 100–500 m) layers. These results suggest that high-resolution models are required for satisfactory reproduction of both nearshore-confined alongshelf transport and subsurface 3-D dispersal of dissolved radionuclides in offshore areas.

A lateral grid resolution of 1 km is widely accepted as the threshold maximum model resolution for adequate representation of submesoscale processes (e.g., Capet et al., 2008a), which is crucial for both the generation of substantially enhanced vertical mixing and the resultant material dispersion in the upper ocean (e.g., Badin et al., 2011; Boccaletti et al., 2007; Callies et al., 2015; Kamidaira et al., 2017; Kunze et al., 2015). The intensities of submesoscale eddies, fronts, and filaments, collectively referred to as submesoscale coherent structures (SCSs) in this paper, vary seasonally with remarkable amplification in the colder season. This is because of mixed-layer deepening and surface cooling that precondition baroclinic instability and symmetric instability near the surface (e.g., Sasaki et al., 2014; Thomas & Taylor, 2010). Because the FNPP1 accident occurred in late boreal winter (March), it could be expected that the SCSs would have influenced the subsequent 3-D mixing and dispersal of the dissolved radionuclides. Note that the approximate scale ranges for SCSs reported in the literature are 0.1–10.0 km horizontally, 0.01–1.00 km vertically, and hours-days temporally (e.g., McWilliams, 2016).

Multiple-nested, very high-resolution (grid spacing: 75 m) downscaling ocean modeling studies (Romero et al., 2013; Uchiyama et al., 2014) have demonstrated that SCSs promote anisotropic, enhanced alongshelf

dispersal of Eulerian passive tracer concentrations and buoyantly neutral Lagrangian particles with minimal cross-shelf dispersal in innershelf and nearshore areas. Both observational and computational studies have shown that SCSs are accompanied by energetic vertical motions, referred to as ageostrophic secondary circulations (ASCs) (e.g., Capet et al., 2008a; Lévy et al., 2001; Mahadevan & Archer, 2000; Nagai et al., 2006, 2012; Pérez et al., 2003; Pollard & Regier, 1992). The kinetic energies of both the mesoscale and the submesoscale are dominated by geostrophy (e.g., Sasaki et al., 2014). However, according to quasi-geostrophic theory, vertical motions depend on the ageostrophic components of the flows rather than on geostrophy. The thermal wind relation also assumes geostrophy in the basic cross-frontal momentum balance, which fails in representing the mixed-layer structure where submesoscale filaments or fronts develop. Gula et al. (2014) proposed that the turbulent thermal wind balance, considering geostrophy and vertical momentum mixing, adequately describes cross-frontal flows in a mixed layer that incorporates overturning circulations (i.e., ASCs). Thus, SCSs comprise along-frontal (or along-filamentary) geostrophic flows and cross-frontal (or cross-filamentary) ASCs (e.g., McWilliams, 2016), and the latter is important to the enhancement of vertical material transport and mixing. ASCs are formed via strong downwelling from zones of surface convergence due to dense (cold) fronts and filaments with peripheral upwelling (McWilliams et al., 2015). Mahadevan and Tandon (2006) found that ASCs in the surface mixed layer occur through frontogenesis, which invokes a temporal increase of the horizontal buoyancy gradient under mesoscale external strain mostly on the flanks of mesoscale eddies. ASCs are considered to interact with mesoscale vertical flows in the surface boundary layer and thus, they enhance vertical mixing. Therefore, given that Tsumune et al. (2012, 2013) were not explicit about the influences of SCSs, we consider that submesoscale eddy-resolving 3-D modeling is important for successful 3-D dispersal realization, particularly in coastal shelf regions such as near the FNPP1. However, the submesoscale influences on the 3-D dispersal of radionuclides, released by the FNPP1 accident, in the coastal shelf area off Fukushima have never been investigated in detail, either observationally or numerically.

In the present study, we developed a submesoscale eddy-resolving oceanic dispersal modeling system for the coastal margin off Fukushima in order to conduct comparative hindcasts of the initial dispersal and subsequent dilution of dissolved ^{137}Cs after the FNPP1 accident, paying particular attention to the influences of SCSs. Our analysis is based on a double-nested ocean downscaling 3-D circulation modeling using the Regional Oceanic Modeling System (ROMS; Shchepetkin & McWilliams, 2005, 2008) embedded within an assimilative oceanic reanalysis, Multivariate Ocean Variational Estimation for the Western North Pacific (MOVE-WNP; Usui et al., 2006) product with lateral grid resolution of 1/10°. Surface wind forcing was provided by assimilative atmospheric reanalysis products, the Grid Point Value of the Global Spectral Model (GPV-GSM; e.g., Roads, 2004) for the parent ROMS (L1) model, and the Mesoscale Model (GPV-MSM; e.g., Isoguchi et al., 2010) for the child ROMS (L2) model. The ROMS-L2 model, which constitutes our principal tool, has 1 km horizontal grid spacing that is considered sufficient for full representation of SCSs. Oceanic 3-D dispersal of the radioactive passive tracer released from the FNPP1 was simulated using the SEA-GEARN-FDM (SGF) Eulerian advection-diffusion model, which was developed at JAEA and designed specifically for oceanic radioactive tracers (Kawamura et al., 2014). Both the direct release and the atmospheric deposition of radionuclides (^{137}Cs) from the FNPP1 are taken into account as point and area sources in the SGF model. Note that the SGF model is a numerical offline Eulerian tracer-tracking model that exploits spatiotemporally interpolated 3-D flow from a circulation model a posteriori. By taking advantage of this functionality, we ran the SGF model to compute ^{137}Cs dispersal with the SCS-resolving ROMS-L2 model and the under-resolving MOVE-WNP model results used for comparative examination of submesoscale effects on ^{137}Cs dispersal. Following the FNPP1 accident, oceanic dissolved ^{137}Cs has been observed intensively (e.g., Aoyama et al., 2016a, 2016b; Buesseler et al., 2017; Kaeriyama et al., 2016; Kumamoto et al., 2017). Thus, we benefited from the availability of abundant ^{137}Cs data for quantitative validation of the coupled circulation-dispersal model.

The remainder of this paper is organized as follows. The modeling framework used for the hindcast experiment for the 4 month period following the FNPP1 accident is described in section 2. Section 3 presents an extensive comparison between the model results, field observations, and satellite altimetry data to validate the model's capability in reproducing oceanic flow fields and radionuclide concentrations. Seasonal variabilities of the submesoscale phenomena and their mechanisms are examined with consideration of eddy energy conversion and spectral analyses in section 4. Section 5 discusses the influences of ASCs associated

with submesoscale eddies in late winter to spring on vertical mixing of ^{137}Cs. To conclude, the summary and discussion are presented in section 6.

2. The Models

2.1. Double-Nested ROMS Model

We used the state-of-the-art ROMS to simulate the circulation off the northeastern Pacific coast of Japan in a double-nested configuration. The ROMS is a free-surface, terrain-following, Primitive-equation 3-D regional hydrodynamic model that incorporates the hydrostatic assumption and the Boussinesq approximation. A versatile first-order boundary turbulence model, the K-Profile Parameterization (KPP) model (Large et al., 1994), was employed to determine the mixed-layer depth (MLD), vertical eddy viscosity, and vertical eddy diffusivity, K_s. Figure 1 shows the hierarchy of the double-nested ROMS model domains (i.e., the intermediate, parent ROMS-L1 and the innermost, child ROMS-L2) embedded within the outermost MOVE-WNP domain. The MOVE-WNP product is an operational numerical reanalysis/forecast product of the Japan Meteorological Agency (JMA) for the northwestern Pacific. It is based on the Meteorological Research Institute Community Ocean Model (MRI.COM) (Tsujino et al., 2010) and it is assimilated with considerable amounts of satellite and in situ data, including Argo profiling float data, using a 3-D variational method. The MOVE-WNP output comprises daily averaged data of sea surface height (SSH), temperature (T), and salinity (S), and meridional and zonal horizontal current velocities. We adapted a one-way offline nesting technique, described in Mason et al. (2010) and in Uchiyama et al. (2014, 2017a, 2017b), to successively reduce the horizontal grid size from ~10 km (MOVE-WNP), to 3 km (ROMS-L1), and then to 1 km (ROMS-L2). The extent of the ROMS-L1 (ROMS-L2) domain was 1,200 × 960 km (704 × 512 km) horizontally with uniform square grid spacing of 3 km (1 km) and 32 vertically stretched layers with refinement near the surface, to encompass the Kuroshio Extension region off Japan. The monthly climatology of freshwater inputs from 14 (8) major rivers in ROMS-L1 (ROMS-L2) was taken into account.

The open boundary and initial conditions of SSH, T, S, and zonal and meridional horizontal current velocities for the ROMS-L1 domain comprised the daily averaged MOVE-WNP data. Model topography was taken from the Shuttle Radar Topography Mission product (SRTM30_Plus) (Becker et al., 2009; Rodriguez et al., 2005), which covers the global ocean at 30 geographic arcseconds (~1 km), supplemented with the J-EGG500 (http://www.jodc.go.jp/data_set/jodc/jegg_intro.html) with 500 m resolution for coastal regions. The GPV-GSM operational atmospheric reanalysis/forecast product of the JMA (horizontal resolution: 0.2° × 0.25°) was applied as daily surface wind stresses in the L1 model. Surface heat, freshwater, and radiation fluxes were given by the monthly climatology of the Comprehensive Ocean-Atmosphere Data Set (COADS)

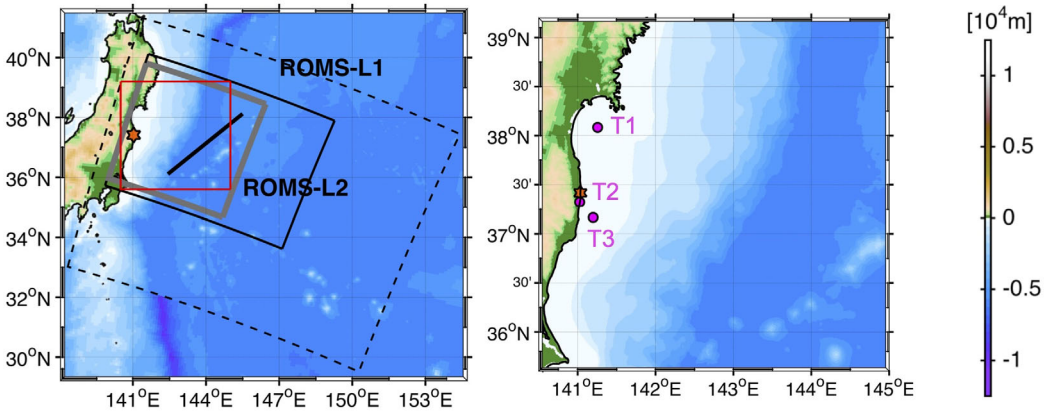

Figure 1. Double-nested ROMS model domains with bathymetry in color for the parent ROMS-L1 (dotted box) and child ROMS-L2 (black solid box) models, embedded within the MOVE-WNP domain (not shown, much wider than the displayed area). Red star indicates the location of the Fukushima Daiichi Nuclear Power Plant (FNPP1). Bold black line identifies the transect for the cross-sectional plots in Figure 4. Gray box is the area used for the spectral analyses in Figure 12. Thin red rectangle corresponds to a zoomed-in region of the SGF-L2 domain (right plot) with the locations of the near-surface monitoring stations (magenta circles) used in Figures 10a–10c. Model domain for SGF-M extends from 10°N–60°N, 120°E–120°W (not shown).

(Woodruff et al., 1987). The 20 day averaged SST and sea surface salinity (SSS) data, obtained from the MOVE-WNP product, were applied for surface flux restoration to avoid long-term drift and bias caused by erroneous surface fluxes from the monthly COADS climatology. The monthly climatology of the major river discharges, compiled by the Japan River Association (http://www.japanriver.or.jp/publish/book/nenpyou_dvd.htm, in Japanese), were applied for all major rivers that discharge in the L1 domain. A four-dimensional TS nudging (*a.k.a.* robust diagnostic) (e.g., Marchesiello et al., 2003; Uchiyama et al., 2017a, 2017b; Wright et al., 2006) with a weak nudging inverse time scale of 1/20 d^{-1} was introduced toward the 10 day averaged MOVE-WNP T and S fields to improve the reproducibility of the Kuroshio path in the L1 domain. The L1 model ran from 1 January 2011 to 1 September 2011.

The innermost ROMS-L2 domain was forced at the lateral open boundaries and it was initialized using the spatiotemporally interpolated 12 hourly averaged L1 output. The 3 hourly surface wind stresses from the JMA GPV-MSM reanalysis were exploited, encompassing the entire L2 domain with horizontal resolution of $0.05° \times 0.0625°$. Similar to the L1 model, the SST and SSS were restored toward the MOVE-WNP SST and SSS as the surface flux correction. The other numerical conditions were the same as the L1 model, although we did not include TS nudging in the L2 model in order to avoid interference with the spontaneous development and decay of intrinsic variability associated with eddies. Surface fluxes other than wind stresses in the L2 domain were also provided by the monthly climatology of the COADS. This choice has been accepted widely in both submesoscale eddy-resolving and submesoscale eddy-permitting model studies with ROMS (e.g., Capet et al., 2008a; Gula et al., 2014; Uchiyama et al., 2017a), whereas more realistic MLD responses might be attained with more elaborate heat flux estimates, such as the bulk formula (e.g., Sasaki et al., 2014). The L2 computational period ran from 11 January 2011 to 1 September 2011. The first 60 days were considered the model spin-up period during which initial adjustment occurred; thus, these data were excluded from subsequent analyses. All statistical analyses conducted in the present study utilized the model results for the same 4 month period (1 March to 30 June 2011) unless stated otherwise. It is worth noting that we did not include tidal forcing because in situ monitoring around the FNPP1 has shown the tidal currents to be weak (Kubota et al., 1981) and insignificant in terms of dispersal (Miyazawa et al., 2012). Furthermore, dispersal and mixing on continental shelves and nearshore areas are affected predominantly by submesoscale stirring rather than by tides (e.g., Romero et al., 2013).

2.2. SEA-GEARN-FDM Model

Oceanic dispersal of the dissolved ^{137}Cs released from the FNPP1 was investigated using the SGF model (Kawamura et al., 2014). The SGF model is an offline Eulerian 3-D advection-dispersion model of arbitrary passive tracers. The source term estimation representing the direct release and the atmospheric deposition of the ^{137}Cs during the accident was implemented as described below. Table 1 lists the numerical configuration of the SGF model. To evaluate the differences in ^{137}Cs dispersal due to the spatial resolution of the flow field, we conducted two SGF runs (i.e., SGF-L2 and SGF-M) by imposing the daily averaged ROMS-L2 (lateral

Table 1
Numerical Configurations of the Two SEA-GEARN-FDM Model Experiments

Models	SGF-L2	SGF-M
Computational period	12 Mar 2011 to 30 Jun 2011, UTC	
Time step	120 s	360 s
Model domain	140.5°E–145°E, 35.6°N–39.2°N	120°E–120°W, 10°N–60°N
Horizontal grid cells	451 × 361	1,200 × 500
Horizontal resolution	0.01°	0.1°
Vertical level (z-coordinate)	79 levels	54 levels
Horizontal diffusivity coefficient	5 $m^2 s^{-1}$	50 $m^2 s^{-1}$
Vertical diffusivity coefficient	KPP	5×10^{-4} $m^2 s^{-1}$
Duration of the oceanic release	26 Mar 2011 to 30 Jun 2011, UTC	
Duration of the atmospheric deposition	12 Mar 2011 to 31 May 2011, UTC	

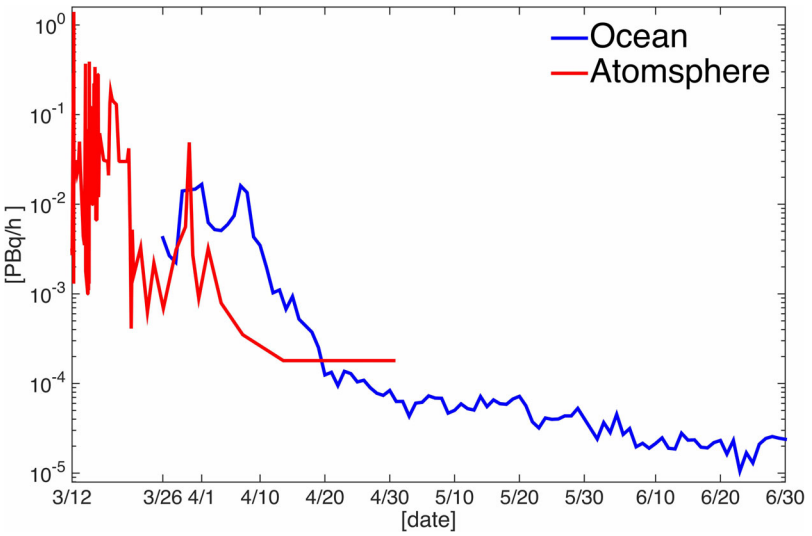

Figure 2. Time series plots of the imposed release rates of ^{137}Cs from 12 March to 30 June 2011. Blue line is the oceanic direct release estimated by Kawamura et al. (2011); red line is the atmospheric release estimated by Katata et al. (2015).

resolution: 1 km) and MOVE-WNP (~10 km) outcomes as input data. The ROMS-L2 (MOVE-WNP) flow fields were interpolated linearly at the 3-D grid points of the SGF-L2 (SGF-M) model with horizontal resolutions of 0.01° ≈ 1 km (0.1° ≈ 11 km) in the latitudinal and longitudinal directions, and 79 (54) vertical z-levels with near-surface refinement ranging from 2 m (1 m) near the surface to 500 m (900 m) near the bed. The daily averaged input field was further interpolated linearly in time to obtain any arbitrary intermediate input data. The KPP-derived tracer vertical eddy diffusivity, K_s, was exploited for the vertical eddy diffusivity of the dissolved ^{137}Cs concentration in the SGF-L2 model. In contrast, a constant value of $K_s = 5 \times 10^{-4}$ m^2 s^{-1} was assumed in the SGF-M model, because the MOVE-WNP product does not include its own K_s. This value of K_s was considered optimal for the present study, according to our preliminary sensitivity test with the SGF-M. We observed that a smaller value of K_s led to degraded ^{137}Cs reproducibility (not shown).

The ^{137}Cs point source introduced as the direct release from the FNPP1 into the ocean was based on in situ ^{137}Cs measurements (Kawamura et al., 2011). We also incorporated atmospheric deposition at the sea surface as the area source of ^{137}Cs based on the Worldwide version of the System for Prediction of Environmental Emergency Dose Information version II (WSPEEDI-II) developed at JAEA (Terada & Chino, 2008). The amount of ^{137}Cs released from 12 March to 30 April 2011, estimated by Katata et al. (2015), was applied as the atmospheric release rate for WSPEEDI-II (Figure 2). The WSPEEDI-II model domain encompassed the SGF-L2 (SGF-M) domain with horizontal resolution of 2 km (10 km) in the latitudinal and longitudinal directions. The 3 hourly (daily) deposition amount of airborne radioactive cesium predicted by WSPEEDI-II was deposited at the sea surface in SGF-L2 (SGF-M) from 12 March to 31 May 2011. Only dissolved ^{137}Cs was taken into account in the present study because it dominated the initial dose inventory, although the SGF model could account for suspended matter such as mineral and biogenic particles that exchange ^{137}Cs with water by absorption and desorption. Note that a truncated half-life of 30 years was used for ^{137}Cs in the SGF model runs because the simulations lasted for only 4 months.

3. 3-D Dynamics and ^{137}Cs Dispersal

3.1. Mean 3-D Dynamics

We compared the double-nested ROMS model results with both satellite data and field observations to validate the reproducibility of the surface dynamics, stratification, and eddy intensity. The AVISO delayed-time mapped absolute dynamic topography from multiple satellite altimetry data (viz., gridded daily composite at 1/4° resolution) (e.g., Le Traon et al., 1998) was used for the mean surface currents, including the Kuroshio. The time-averaged surface current velocity magnitude from the ROMS-L2 model, overlaid on that from the ROMS-L1 model, shows reasonable quantitative agreement with the satellite observations in terms

of both magnitude and spatial patterns, including the meandering Kuroshio path (Figures 3a and 3b). The SSH variance is shown in Figures 3c and 3d as a proxy for the temporal variability of the synoptic and mesoscale signals. An overall agreement is exhibited between the modeled SSH variance and that of AVISO. For instance, both variances are intensified considerably around the Kuroshio and its Extension Jet, corresponding to the meandering path of the Kuroshio.

The modeled stratification was compared with the XBT-DBT observations acquired by the JMA's survey ship, the R/V *Ryofu Maru* (http://www.data.jma.go.jp/gmd/kaiyou/db/vessel_obs/data-report/html/ship/cruisedata_e.php?id=RF1107), along the transect off Fukushima that is represented by the bold black line in Figure 1. Snapshots of temperature in the vertical cross section on 6 June 2011, from the L2 model and the JMA observations are consistent, indicating a tilted thermocline around the Kuroshio from 36.2°N to 36.8°N (Figures 4a and 4b). The time-averaged Kuroshio main body exists from 36.2°N to 37.2°N with mean streamwise velocities of <0.3 m s^{-1}, even at the depth of 400 m, consistent with previous studies (e.g., Qiu, 2001) (Figure 4c). Hence, the deep thermocline at around 36.2°N reflects the subtropical warm water brought by the Kuroshio. The temporal standard deviation (RMS) of vertical velocity w is magnified around the Kuroshio main body and near the base of the time-averaged mixed layer on the northern side of the Kuroshio (Figure 4c). In turn, the time-averaged K_s estimated by the KPP model is large mostly on the northern side of the Kuroshio at O (10^{-3} m^2 s^{-1}) in the upper ocean, which is three orders of magnitude larger than the background diffusivity of O (10^{-6} m^2 s^{-1}) in the ocean interior (Figure 4d). These results demonstrate that the vertical advective transport and vertical eddy diffusion through K_s are concurrently responsible for vertical mixing in the upper ocean, whereas the former is anticipated to prevail in the vertical transport into the ocean interior below the mixed layer and near the Kuroshio. Apparently, the constant value of K_s used in the SGF model (section 2.2) is ad hoc, which introduces uncertainty in the dispersal modeling even though our choice of K_s provides reasonable reproducibility for ^{137}Cs (section 3.3). The introduction of an offline turbulent closure model could provide a more plausible estimation of K_s for use in the SGF model. However, this is beyond the scope of the present study and we leave this issue for future work.

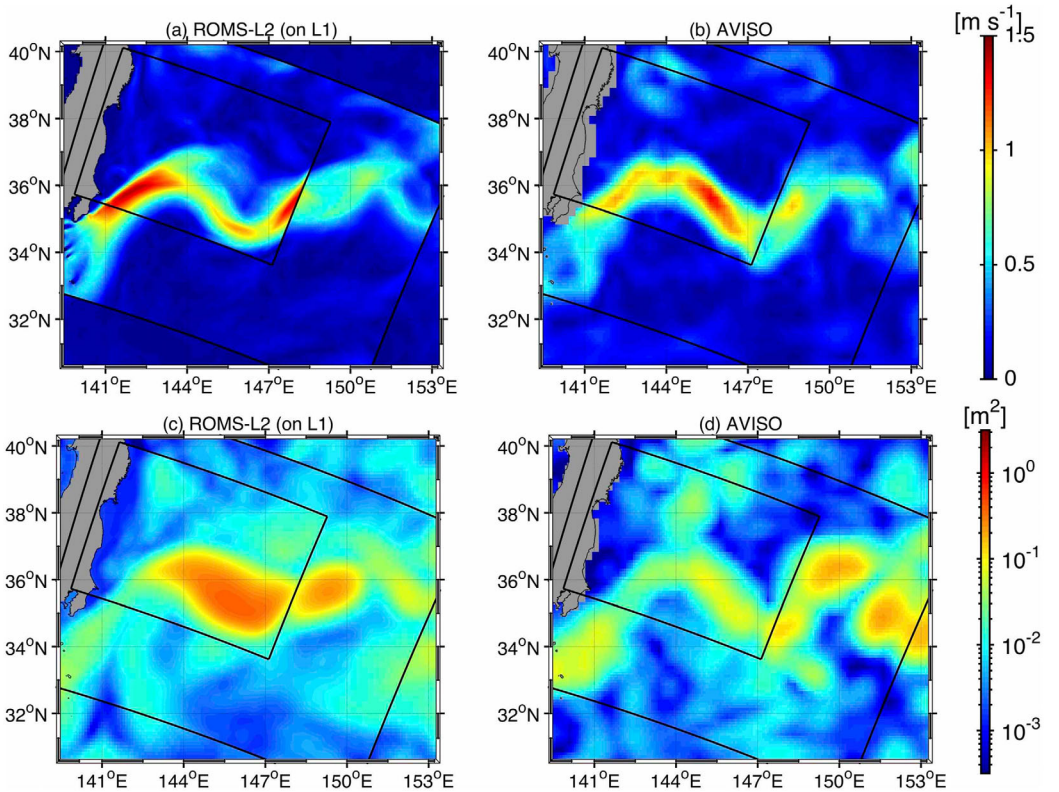

Figure 3. Plan view plots of (a and b) time-averaged surface velocity magnitude, and (c and d) sea surface height (SSH) variances. Left plots (a and c) are the ROMS-L2 result superposed on the L1 result, while right plots (b and d) are based on AVISO satellite altimetry.

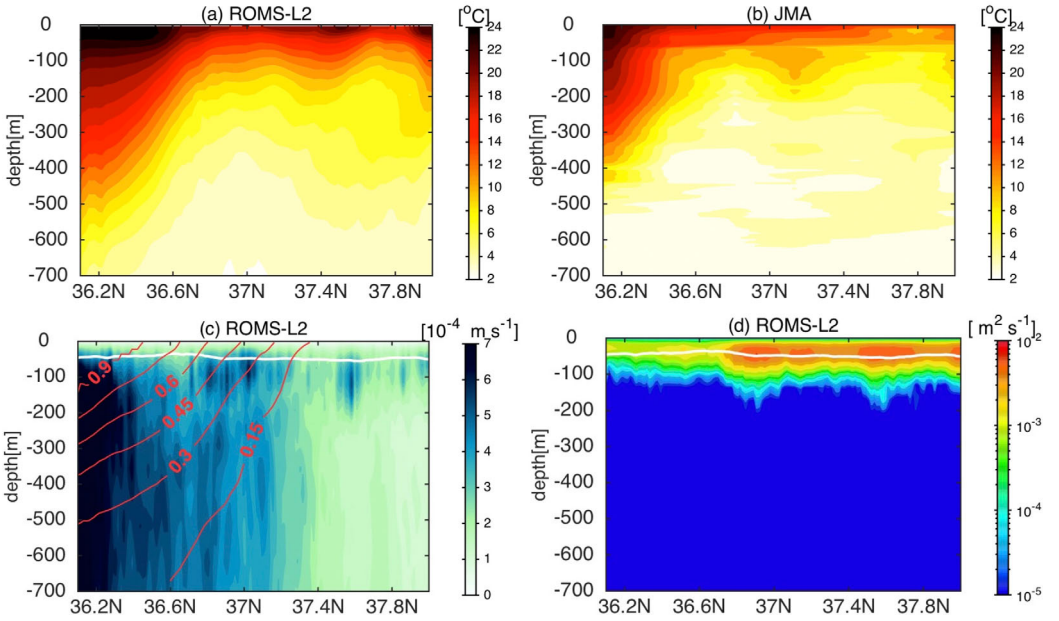

Figure 4. Cross-sectional plots of (a and b) snapshots of temperature from the ROMS-L2 model and JMA observation, (c) mean streamwise velocity at intervals of 0.15 m s^{-1} normal to the transect (red contours) and temporal standard deviation (RMS) of vertical velocity, w (color) from the ROMS-L2, and (d) time-averaged vertical eddy diffusivity, K_s, estimated by the KPP model, along the transect shown by the bold black line in Figure 1. White curves in the bottom plots are time-averaged mixed-layer depths (MLDs) estimated by the KPP model.

3.2. Eddies

To validate the time-dependent reproducibility of the model, we examined the surface eddy kinetic energy (EKE):

$$K_e = \frac{1}{2}\left(\overline{u'^2} + \overline{v'^2}\right), \tag{1}$$

where (u, v) is the horizontal (zonal and meridional) velocity, and the overbar represents an ensemble-averaging operator. The variables assigned with the prime are the fluctuating eddy components obtained by removing the seasonal variations with a low-pass Butterworth filter in the frequency domain with a 90 day cutoff period. Figures 5a and 5b indicate that K_e from the ROMS and MOVE-WNP are similar in their overall spatial patterns, where intensification of K_e occurs around the Kuroshio path; however, the magnitudes are somewhat different. In the ROMS, K_e is increased because the lateral grid resolution is increased for better resolution of the buoyancy gradients and the associated velocity shear, which results in higher EKE, particularly around the Kuroshio front.

The differences in the K_e magnitude are clearly illustrated in snapshots of the daily averaged surface relative vorticity, normalized by the local Coriolis frequency f, as contrasting emergence of mesoscale and submesoscale eddies on 2 April 2011, from the ROMS and MOVE-WNP models (Figures 5c and 5d). The two models commonly yield positive and negative vortex streamers on the mesoscale at O (100 km), corresponding to the Kuroshio. However, submesoscale eddies at O (1–10 km) develop much more prominently in ROMS-L2 than MOVE-WNP, which shows that the higher-resolution L2 model generates much finer submesoscale eddies. The eddies and associated SCSs in the L2 model have greater magnitudes, are distributed more extensively, and are more diversified and strengthened than those in MOVE-WNP, all of which coincide with the resultant K_e distributions (Figures 5a and 5b). As shown in Figure 6, the SCSs in the L2 model are accompanied by intensive vertical motions, as shown in the cross-sectional snapshot of the daily averaged vertical velocity w along the transect defined offshore from the FNPP1 indicated by the bold blue line in Figure 5b. In turn, vertical flows are extremely small in the MOVE-WNP model. The intensified w is produced in the surface mixed layer as ASCs due to SCSs (e.g., Capet et al., 2008a). The SCSs and ASCs develop more intensively in the colder seasons from winter to spring with the MLD deepening (e.g., Sasaki et al., 2014), as is examined

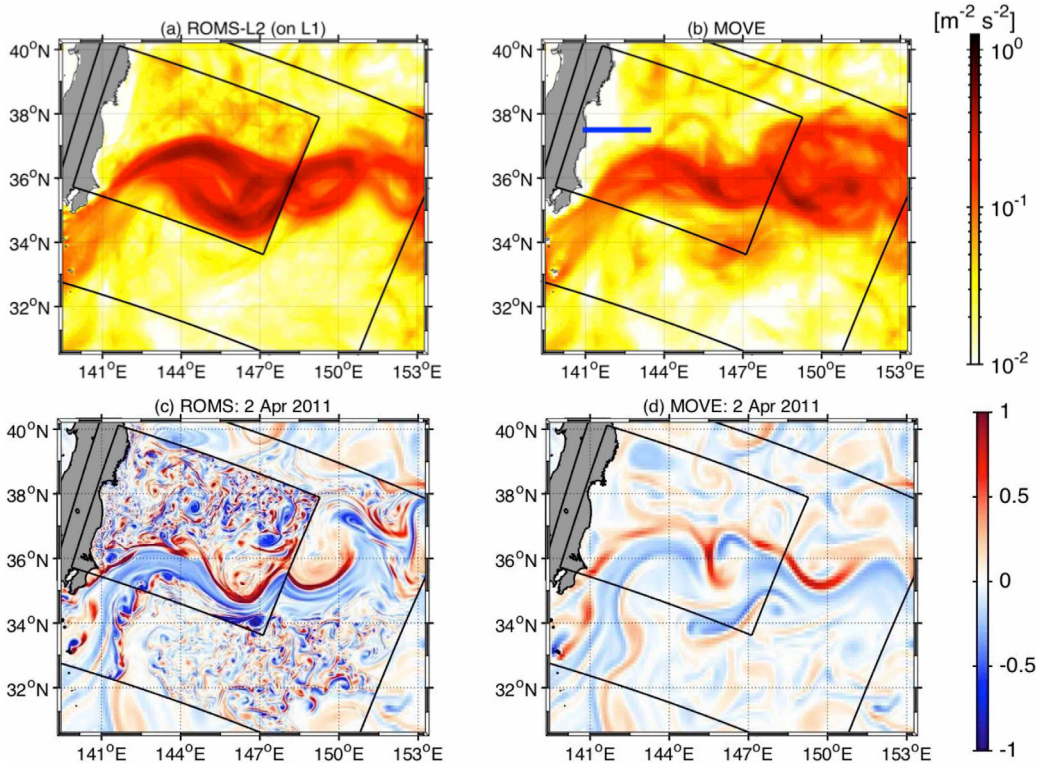

Figure 5. (top) surface eddy kinetic energy (EKE), K_e, from (a) the ROMS-L2 on L1, and (b) MOVE-WNP reanalysis. (bottom) Daily averaged spatial distributions of surface vertical relative vorticity normalized by planetary vorticity (dimensionless) on 2 April 2011 from (c) the ROMS-L2 on L1, and (d) MOVE-WNP models. Blue thick line in Figure 5b identifies the transect used for the cross-sectional plots in Figure 6.

in detail in section 4.3. In summary, the present double-nested ROMS model is shown to have satisfactory reproducibility in terms of the synoptic and mesoscale dynamics, including the Kuroshio with the prominent amplification of the submesoscale variability overlaid.

3.3. Dissolved Radionuclides

We verified the modeled ^{137}Cs concentrations against a variety of observed data based on in situ water sampling. Because the present study focuses on the initial dispersal and the dilution of ^{137}Cs after the FNPP1 accident, we used the "best available" offshore ^{137}Cs dataset for June 2011 (Buesseler et al., 2012) for the 3-D spatial distribution. To consider the temporal variation, we used nearshore surface ^{137}Cs data from mid-March to the end of June 2011, collected intensively near the FNPP1 by the Tokyo Electric Power Company (TEPCO) (http://www.tepco.co.jp/en/nu/fukushima-np/f1/index2-e.html). The horizontal ^{137}Cs

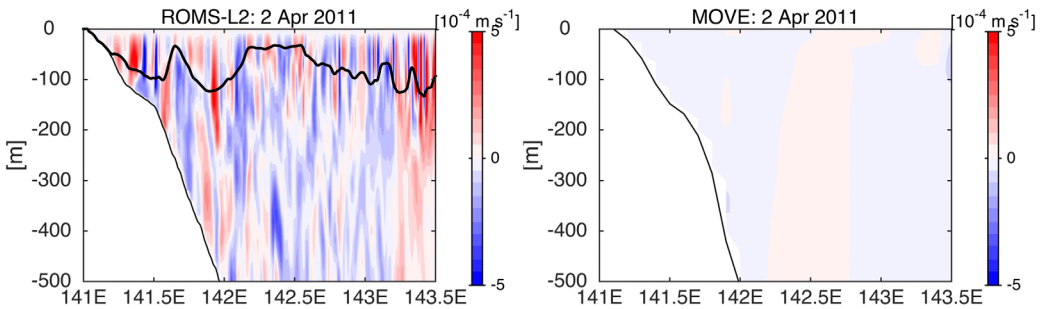

Figure 6. Cross-sectional plots of the daily averaged vertical upward velocity, w, from the (left) ROMS-L2 and (right) MOVE-WNP models. Black line in the left plot is the mixed-layer depth (MLD) estimated by the KPP model. The corresponding transect is shown by the blue line in Figure 5b.

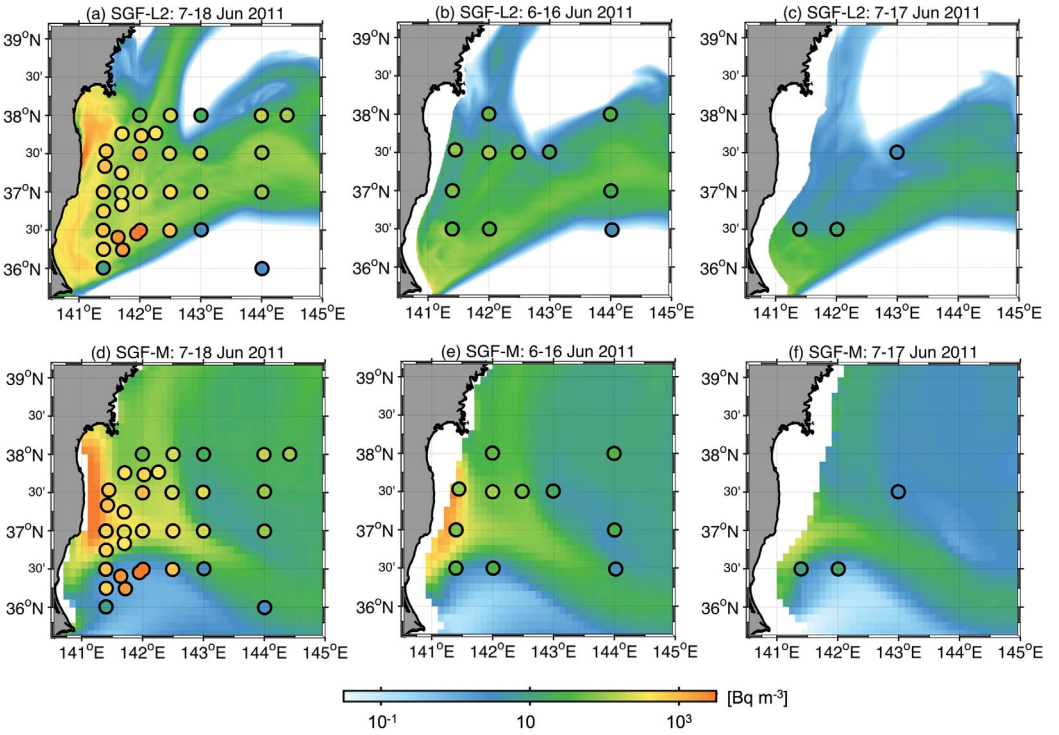

Figure 7. Modeled ^{137}Cs concentrations (color) from the (top plots) SGF-L2 and (bottom plots) SGF-M models at (a and d) the surface, (b and e) 100 m depth, and (c and f) 200 m depth. Colored circles indicate the instantaneous in situ concentrations (Buesseler et al., 2012) using the same color scale.

distributions are compared at the surface and at depths of 100 and 200 m for the two model results (i.e., SGF-L2 and SGF-M) with the measured data superposed as colored circles in Figure 7. Here we show only the measured ^{137}Cs considered derived from the FNPP1, which can be determined from the detection level of another isotope, ^{134}Cs. The number of available observed data in Buesseler et al. (2012) was only 87. Overall, the two models reproduced the observations reasonably well, presenting high concentrations near the shore with alongshelf spread and downward decreasing trends; however, they are not perfect. The SGF-L2 generally outperforms SGF-M with an improvement of the model skill score (Wilmott, 1981) from 0.2917 to 0.3494 (*n.b.*, model skill score is 1 for perfect agreement and 0 for complete disagreement). Even though the bulk of the hydrodynamics evaluated by ROMS-L2 and MOVE-WNP are closely related, as discussed in sections 3.1 and 3.2, the resultant ^{137}Cs levels are distributed quite differently. The surface ^{137}Cs from SGF-L2 is more comparable with the observed data, especially near the coast and the Kuroshio path (Figure 7a). In contrast, the offshore transport manifest by SGF-M is more prominent, and is subsequently entrained by the Kuroshio. The slight deviation of the predicted location of the Kuroshio, i.e., a northward shift of about 50 km (~0.5°) relative to that of the SGF-L2, promotes intense dilution in the coastal area off the FNPP1 and remarkable underestimation south of ~36.5°N (Figure 7b). Similarly, the subsurface ^{137}Cs from SGF-L2 shows reasonable agreement (Figures 7b and 7c), whereas SGF-M yields unrealistically high levels of ^{137}Cs near the coast, in particular at 100 m depth (Figures 7e and 7f). According to an observational study (Aoyama et al., 2012), an anticyclonic mesoscale eddy centered at 36.5°N, 141.4°E in mid-May 2011 might have prevented southward alongshelf transport of ^{137}Cs. Consistent with Aoyama et al. (2012), SGF-L2 manifests southward coastally trapped alongshelf transport of ^{137}Cs after the end of May 2011, when the anticyclonic mesoscale eddy was suppressed by a tropical cyclone (not shown).

A similar conclusion can be drawn from the vertical cross-sectional views of ^{137}Cs along the offshore transect from the FNPP1 (blue line in Figure 5b) in Figure 8. Although both models reproduce the 3-D ^{137}Cs distribution moderately well for June 2011 (Figures 8a and 8b), the SGF-M model overestimates the downward ^{137}Cs transport. This results in higher concentrations at depth, partly because of our choice of the vertical diffusivity K_s. The SGF-M also indicates an almost uniform pattern of ^{137}Cs dilution in the offshore and

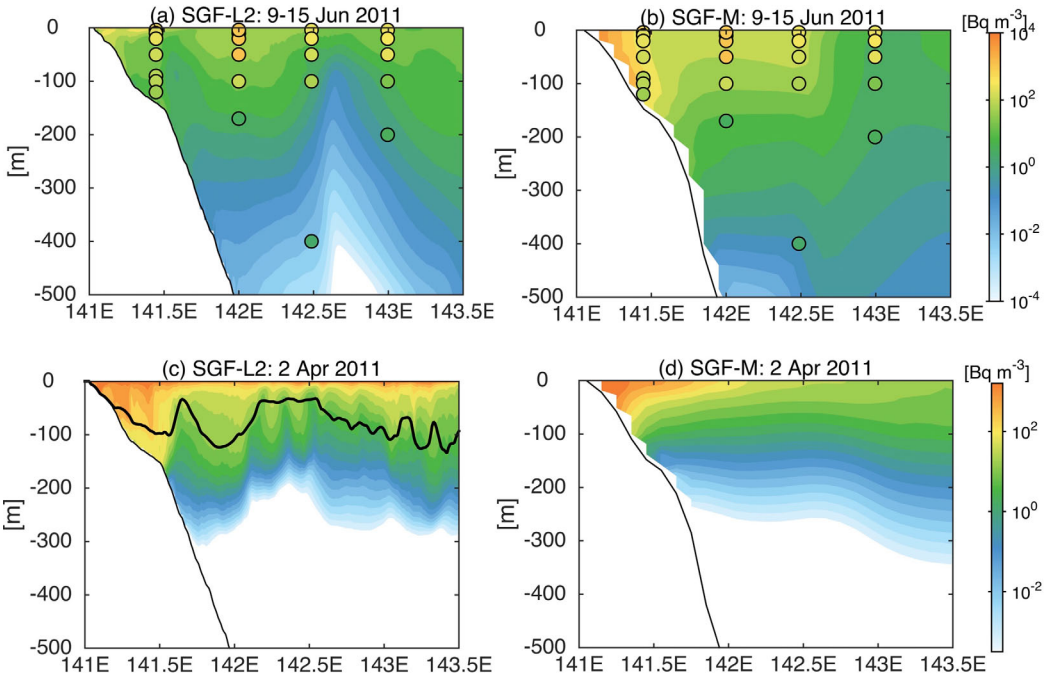

Figure 8. Cross-sectional plots of ^{137}Cs concentrations from the (left) SGF-L2, and (right) SGF-M. (top) Time-averaged ^{137}Cs from 9 to 15 June, and (bottom) the daily averages for 2 April. Colored circles in top plots indicate instantaneous in situ concentrations measured in June 2011 (Buesseler et al., 2012). Black curve in Figure 8c is the mixed-layer depth estimated by the KPP model. The corresponding transect is shown by the blue line in Figure 5b.

downward directions due to intense lateral (isopycnal) advection and large vertical (diapycnal) diffusion. In contrast, the SGF-L2 has greater patchiness, as evidenced by the near-surface peak concentrations at 142°E and 143°E. These results suggest the coarse-resolution SGF-M model is rather "diffusive" with transport that is spatially more homogeneous because of the poor representation of w, which is compensated by strong vertical diffusion via the imposed K_s. The scatter diagram of modeled versus measured ^{137}Cs, shown in Figure 9, illustrates that both the SGF-L2 and the SGF-M slightly underestimate the observed concentrations. The results of a supplemental numerical experiment without atmospheric release suggested that this underestimation could be caused by errors in the direct oceanic release rate estimation (not shown), in conjunction with the omission of the outgoing ^{137}Cs returning to the L2 domain in SGF-L2, rather than possible errors in the atmospheric source term estimation. However, a large proportion of the modeled ^{137}Cs from SGF-L2 is within the range of a factor of 10, indicated by the dotted lines relative to the measured ^{137}Cs, with an apparent improvement for higher concentrations of ^{137}Cs > 1 Bq m^{-3}, compared with SGF-M, which underestimates the measured ^{137}Cs considerably. The improvement with SGF-L2 is quantified by the rate of the modeled ^{137}Cs within the range of a factor of 10 of the measured ^{137}Cs. This rate computed with all 87 data improved from 67.8% (SGF-M) to 71.3% (SGF-L2), while that at depths ≧100 m (with only 19 data) improved from 68.4% (SGF-M) to 73.7% (SGF-L2).

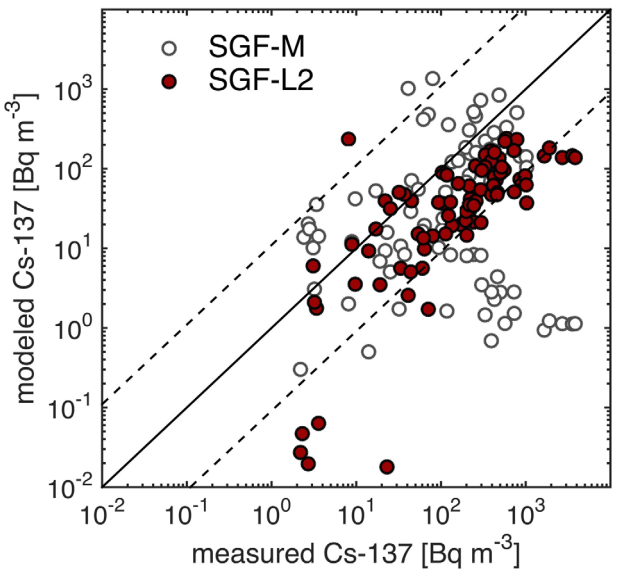

Figure 9. Scatter diagram of the ^{137}Cs concentrations from the SGF-M (white circles) and SGF-L2 (red circles) models against in situ sampled data (Buesseler et al., 2012). Error bars are quite small as they are within the size of the symbols, and thus not shown here. The solid line represents the 1:1 correlation and it is bounded by two dashed lines indicating the deviations with factors of 1/10 and 10.

These results demonstrate that the high-resolution SGF-L2 outperforms the coarse-resolution SGF-M in the overall reproducibility of ^{137}Cs. A plausible reason for a more successful hindcast using SGF-L2 is the usage of a finer lateral grid resolution, which allows more realistic representation of SCSs and ASCs (sections 3.1 and 3.2). We might

be able to improve the SGF-M model by tweaking the background K_s and avoiding laborious high-resolution modeling (see also section 3.1). To investigate the influence of SCSs, we examined the cross-sectional views of ^{137}Cs in April 2011, i.e., when SCSs are most pronounced. As shown in Figures 8c and 8d, the SGF-L2 results in more intensified levels of ^{137}Cs near the surface. These extend offshore from the coast with notable cross-shelf variability at cross-shelf wavelengths of 5–20 km, accompanied by downward penetration beyond the base of the mixed layer via intense ASCs. In contrast, the SGF-M yields a diffusive distribution of ^{137}Cs with high concentrations remaining near the coast. Hence, it is confirmed that SCSs and ACSs have considerable effect on the 3D dispersal of ^{137}Cs, particularly in the colder months (i.e., March and April 2011) that correspond to the initial period shortly after the FNPP1 accident. Obviously, the degraded estimates using SGF-M can be attributed to the coarse-resolution MOVE-WNP, which does not account properly for the SCSs but instead requires a tweak of K_s that introduces large uncertainty. However, the SGF-L2 does have a downside in that some areas are assigned zero ^{137}Cs near the northern and southern open boundaries (Figure 7). This is because we did not consider outgoing ^{137}Cs returning to the L2 domain. However, this deficiency could be improved by introducing a nested SGF configuration.

3.4. Temporal Variability

Figures 10a–10c compares temporal variations of near-surface ^{137}Cs from the two models and measurements conducted by TEPCO (http://www.tepco.co.jp/en/nu/fukushima-np/f1/index2-e.html) at three stations near the FNPP1, as indicated in the inset in Figure 1. In general, both models provide reasonable agreement with the measurements. Model skill scores between the model results and the measurements conducted by TEPCO, including those at the three stations, from 13 March to 30 June 2011, are improved considerably from 0.1244 (SGF-M) to 0.6930 (SGF-L2). The SGF-L2 produced a greater number of apparent temporal fluctuations for periods of several days, most likely coinciding with eddying flows that promote intense downward transport (Figures 6 and 8). Temporal variations of the modeled ^{137}Cs inventory in the SGF-L2 model domain were then estimated using the volume integral of ^{137}Cs, normalized by the total amount of FNPP1-derived ^{137}Cs for the 4 month period (Figure 10d). Because the inventory integrated from the surface down to the depth of 100 m is about the same as that down to the depth of 1000 m, the released ^{137}Cs exists mostly in the upper ocean. The SGF-L2 result indicates that the surface mixed layer stores 53% of the released ^{137}Cs in the first several weeks. The ^{137}Cs inventory evaluated from the SGF-M model is generally smaller than that from SGF-L2 until the end of April. This is because the SGF-M gives rise to more prominent offshore transport, which is subsequently entrained by the Kuroshio (section 3.2). However, after 30 April, the initial dilution is more evident in SGF-L2 because the SGF-M model results retain high ^{137}Cs concentrations near the coast, whereas SGF-L2 might overestimate the dilution, partially because of the lack of reentering ^{137}Cs. The area-averaged KPP-estimated MLD represents a nearly monotonic decrease with time, where late winter conditions are attributed to a deeper MLD (Figure 10e). Figure 10f shows a time series of the surface K_e (EKE), volume-averaged laterally over the SGF-L2 domain and from the surface to a depth of 400 m vertically. The K_e fluctuates similarly in the two circulation models with overall intensification in the high-resolution ROMS-L2 model compared with MOVE-WNP, particularly in the first month and in June. Because MOVE-WNP is exploited to force the ROMS-L1 and L2 models, the intensified K_e is generated intrinsically because of the grid refinement.

These results suggest that near-surface model-data comparison would be insufficient for model validation and for source term estimation. This is because the SGF-L2 result indicates that significant vertical transport of ^{137}Cs due to eddies and associated vertical flows are anticipated to alter markedly the surface distribution of ^{137}Cs. Therefore, a higher-resolution model is needed for a more accurate representation of the vertical mixing of ^{137}Cs, which is sensitive to eddying and transient ambient flows that are largely affected by the seasonally varying MLD. In summary, we confirmed that the double-nested ROMS coupled with the SGF (viz., SGF-L2) model was satisfactory in reproducing the 3D dispersal and initial dilution of dissolved ^{137}Cs originating from the FNPP1 accident. The open boundary artifact causing the long-term dilution of ^{137}Cs in the SGF-L2 could be improved if desired. We should emphasize that the SGF-M model is better suited than SGF-L2 to basin-scale and long-term analyses, whereas the high-resolution model definitely outperforms the former near the center of the accident and in coastal shelf regions, producing higher accuracy in the 3-D representations of short-term dispersal.

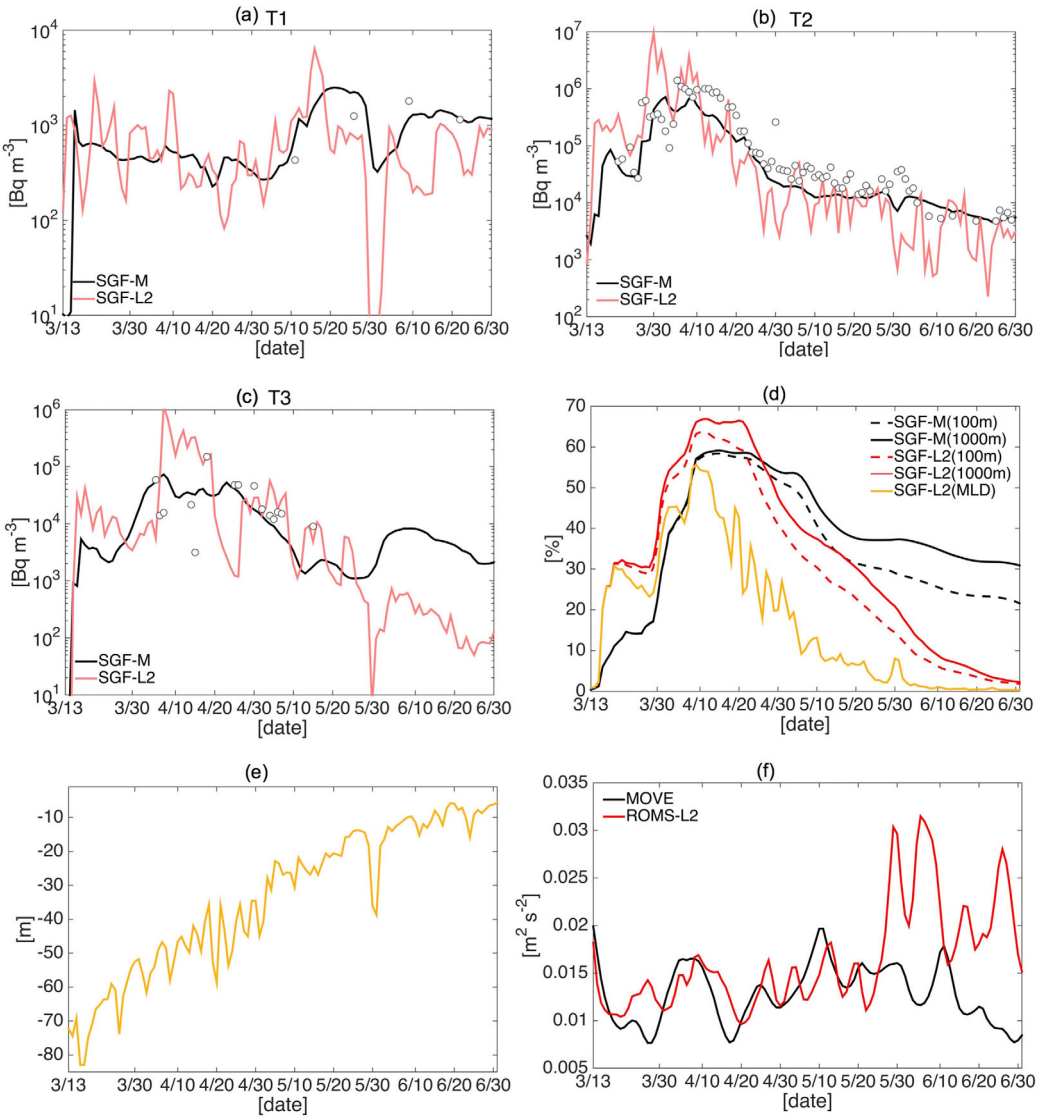

Figure 10. Time series plots of various quantities. Near-surface ^{137}Cs concentrations from the SGF-M (black) and SGF-L2 (red) models, and measured data (white circles) around the FNPP1 at (a) T1, (b) T2, and (c) T3. The uncertainties of the observations by TEPCO are not reported. Locations of the measurements are shown in Figure 1. (d) Inventory (the total amount) of ^{137}Cs in the SGF-L2 model domain, integrated vertically from the surface down to the labeled depths ($z = -100$ m, $-1{,}000$ m, and the base of the surface mixed layer denoted by MLD) normalized by the total ^{137}Cs load derived from the FNPP1 as the sum of the oceanic direct release and atmospheric deposition. (e) Spatial MLD estimated by the KPP model of the ROMS-L2. (f) Volume-averaged surface ($z > -400$ m) eddy kinetic energy, EKE (K_e), for the SGF-L2 domain.

4. Submesoscale Dynamics

4.1. Extraction of Submesoscale

SCSs in the North Pacific are known to have strong seasonality, with much greater energetic variability in colder seasons than in warmer seasons, and mixed-layer deepening (Figure 10e) plays an important role in the development of SCSs and ASCs (e.g., Sasaki et al., 2014). To separate submesoscale variability from the eddy component of any modeled prognostic field, we introduced a horizontal spatial filter. This incorporated a convolution of the 2-D Gaussian smoothing kernel function, computed with a diameter of 20 km (viz., discrete 21 × 21 grid points for the ROMS-L2 and SGF-L2 models) relative to each model grid point and a standard deviation of 4.5 km. This means that length scales shorter than ~20 km constitute our definition of the submesoscale structures to be isolated. The variable V is thus decomposed as:

$$V=\overline{V}+V';\ V'=V'_m+V'_s, \tag{2}$$

where $\overline{V}$ and V' are the seasonal and eddy components, respectively, as defined in section 3.1, and subscripts m and s represent the mesoscale and submesoscale components, respectively, decomposed by the 2-D Gaussian filter.

4.2. Seasonal Variability

The monthly averaged surface submesoscale EKE from ROMS-L2 (Figures 11a–11c) shows that the EKE is greatest in April 2011, not only around the mean Kuroshio path indicated by the blue contours for velocity magnitude, but also in an extensive area to the north of the Kuroshio that includes the coastal area. The associated vertical velocity variance $\overline{w'^2}$ at the MLD (i.e., base of the surface mixed layer, Figures 11d–11f) varies consistently with the EKE, where $\overline{w'^2}$ is also largest in April, which is attributed to ASCs associated with SCSs. We then estimated the azimuthally averaged wave number spectra of the surface horizontal velocity (i.e., kinetic energy spectra; Figure 12a) and the vertical velocity at the MLD (Figure 12b) for the subdomain defined by the gray square in Figure 1 for each of the 3 months from April to June 2011. The spectral computations were performed offline using daily averaged values from ROMS-L2, with subtracting the spatial mean values over the area used for the spectral analyses (the gray square in Figure 1) to define fluctuating components. Two-dimensional wave number spectra were determined daily by a 2-D FFT with the azimuthal averaging operation posteriori, and then temporally averaged for each month. The maximum resolved wavelength is 450 km, while the Nyquist wavelength is 2 km.

The surface kinetic energy spectra have similar shapes for the 3 months; however, the spectral slope is gentle in April with temporal steepening occurring until June (Figure 12a). In April, the spectral power is highest at higher wave numbers and lowest at lower wave numbers. This indicates that kinetic energy in the submesoscale range is higher in April than in other months. The spectral slope is close to k^{-3} rather than k^{-2} for higher wave numbers, where the latter has been observed in fully developed submesoscale turbulent regimes (e.g., Capet et al., 2008a). Figure 12b shows more striking submesoscale dominance in the upper ocean. Similar to Figure 12a, the w spectrum in April is notably enhanced for a notably extensive wave number range, peaking at wavelengths of about 10–20 km (viz., submesoscale), even with the deepest mixed layer among the first 3 months after the accident (Figure 10e). These results are consistent with the spatial distributions of the submesoscale EKE and $\overline{w'^2}$ shown in Figure 11. Therefore, submesoscale variability was

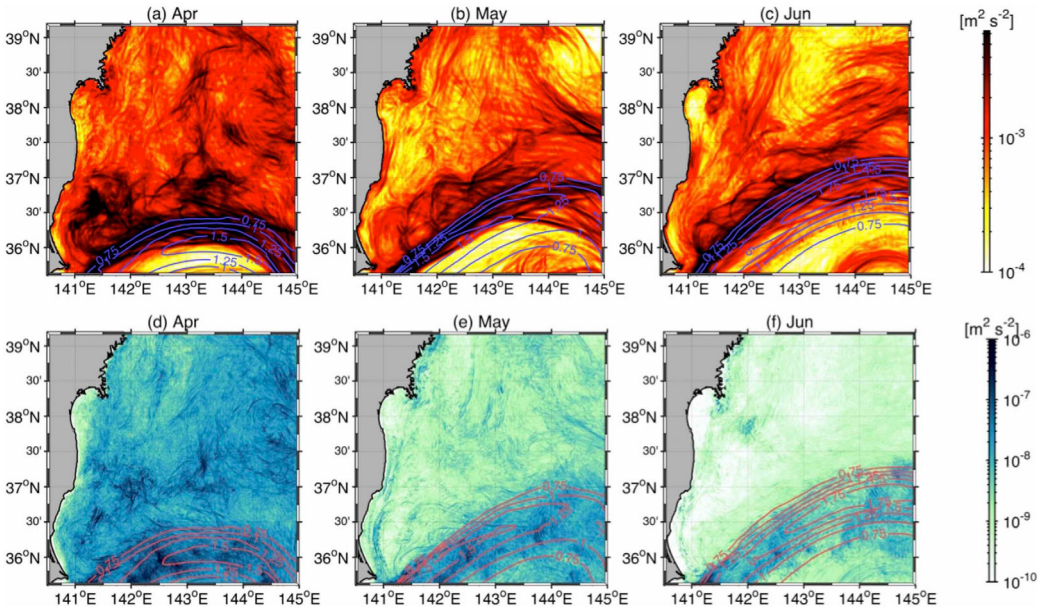

Figure 11. (top) Monthly averaged surface submesoscale EKE from the ROMS-L2 for (a) April, (b) May, and (c) June 2011. (bottom) Submesoscale vertical velocity variance $\overline{w'^2}$ at the mixed-layer depth (MLD) from the ROMS-L2 for (d) April, (e) May, and (f) June 2011. Contours represent monthly averaged surface velocity magnitude at intervals of 0.25 m s^{-1}, depicting the monthly averaged Kuroshio path.

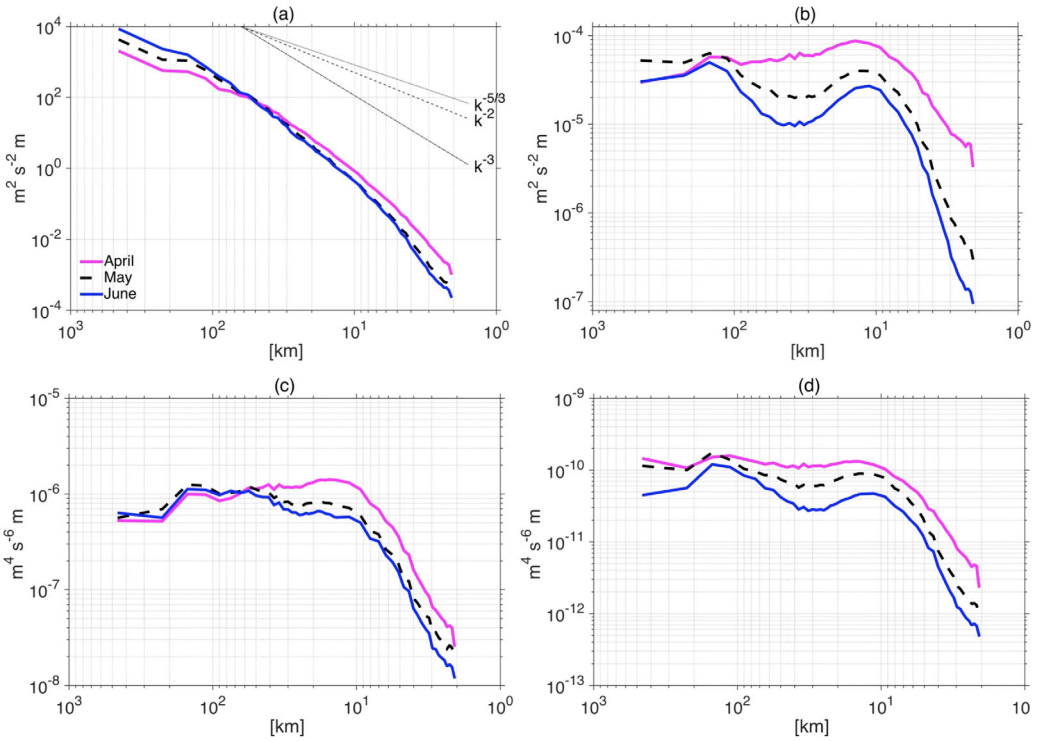

Figure 12. Wave number spectra of (a) kinetic energy at the surface, (b) vertical velocity at the mixed-layer depth (MLD), (c) barotropic conversion rate, K_mK_e, averaged vertically over the surface mixed layer, and (d) baroclinic conversion rate, P_eK_e, averaged vertically over the surface mixed layer. Curves are for each of the 3 months from April to June 2011. Straight lines indicate the spectral slopes of $k^{-5/3}$ (black), k^{-2} (dashed), and k^{-3} (gray), where k is the wave number.

still evident with reasonably intense ASCs in April 2011, although it was slightly weakened from the fully developed stage that perhaps occurred in January and February. These results also confirm that the combination of the COADS climatological heat, freshwater, and radiative surface fluxes with the realistic GPV-MSM wind stresses may be able to reproduce the development of SCSs and ASCs to some extent (see also section 2.1). In addition, the w spectra have a secondary peak near the wavelength of 100–200 km (viz., mesoscale), which confirms that both mesoscale and submesoscale variability concurrently influence vertical mixing in the upper ocean.

4.3. Eddy Generation Mechanisms

To investigate a possible cause of the instability and the eddy-mean interaction mechanisms, we examined the energy conversion rates in the K_e (EKE) conservation equation (e.g., Dong et al., 2007; Kamidaira et al., 2017; Klein et al., 2008; Marchesiello et al., 2003;). In this study, we focus on the two most important quantities: the release of eddy available potential energy (P_e) to feed K_e (P_eK_e), and the work done by the Reynolds stress on the mean velocity shear (K_mK_e), which represents the energy exchange between the mean kinetic energy (K_m) and K_e (EKE):

$$K_mK_e = -\left(\overline{u'u'}\,\frac{\partial\overline{u}}{\partial x} + \overline{u'v'}\,\frac{\partial\overline{u}}{\partial y} + \overline{u'w'}\,\frac{\partial\overline{u}}{\partial z} + \overline{v'u'}\,\frac{\partial\overline{v}}{\partial x} + \overline{v'v'}\,\frac{\partial\overline{v}}{\partial y} + \overline{v'w'}\,\frac{\partial\overline{v}}{\partial z}\right), \tag{3}$$

$$P_eK_e = -\frac{g}{\rho_0}\overline{\rho'w'}, \tag{4}$$

where x, y, and z are the horizontal and vertical coordinates, ρ is the density of sea water, $\rho_0 = 1027.5$ kg m^{-3} is the Boussinesq reference density, and g is gravitational acceleration. If the barotropic conversion (or shear production) rate $K_mK_e > 0$, then barotropic and vertical shear instability occurs, destabilizing the mean flow to generate eddies; thus, K_e increases. In contrast, when the baroclinic conversion rate $P_eK_e > 0$, baroclinic

instability takes place to magnify K_e. On the other hand, negative K_mK_e (P_eK_e) corresponds to coalescence of eddies (restratification) that leads to flow stabilization.

Following the analysis of Sasaki et al. (2014), we examined the wave number spectra of K_mK_e and P_eK_e for each of the first 3 months averaged vertically over the surface mixed layer to investigate the scales involved in the K_e source in the upper ocean (Figures 12c and 12d). Evident similarities are observed in both the spectra as well as the w spectra (Figure 12b). The spectral power is highest in April with a decreasing trend with time. A distinctive primary peak appears at the wavelengths of about 10–20 km (i.e., submesoscale), particularly in K_mK_e in April. Another spectral peak is centered on the wavelengths of about 100–200 km (i.e., mesoscale), which largely dominates over the submesoscale spectral peak in the 2 warmer months. Based on a submesoscale eddy-permitting simulation of the North Pacific at the horizontal resolution of 1/30° (~3 km), Sasaki et al. (2014) qualitatively drew the same conclusion, where the winter (summer) spectrum peaks were found at the wavelength of about 30 km (125 km). Although their peak wavelengths are somewhat different from those of the present study, mainly because of differences in the 1 km versus 3 km lateral grid resolution and in the coastal versus offshore setting, the modeling of both works demonstrates that submesoscale ASCs in the mixed layer develop most energetically in colder months (i.e., April 2011 for the present analysis). This is because shear instability acts as the primary K_e source to submesoscale variability, with baroclinic instability acting as the secondary K_e source. It should be noticed that the mean K_mK_e and P_eK_e are about the similar magnitudes (not shown), whereas their wave number spectra are quite different because K_mK_e varies in space much more significantly than P_eK_e around the Kuroshio path. It is worth noting that these results are slightly different from those of Sasaki et al. (2014) and Capet et al. (2008b), who concluded that baroclinic instability is the primary K_e source rather than shear instability, because our study area contains the vigorous background current, viz., the Kuroshio, and the nearshore region much more extensively than those of Sasaki et al. (2014) and Capet et al. (2008b). Such conditions are, respectively, responsible for enhancing shear instability associated with intense lateral shear and topographic eddy shedding as suggested in previous works (e.g., Dong et al., 2007; Kamidaira et al., 2017; Uchiyama et al., 2017a).

5. Vertical ^{137}Cs Flux

ASCs induced by submesoscale eddies are anticipated to promote vertical mixing and resultant vertical tracer transport. The SGF-L2 model manifests that ^{137}Cs mostly remains in the upper ocean (Figure 10d) and serves as the source of the downward ^{137}Cs flux. The vertical diffusive ^{137}Cs flux, $-K_s\partial_z C$, is three to four orders of magnitude smaller than the advective flux; thus, we omit it in the following analysis. Specifically, on average, the diffusive flux at $z = -100$ m is merely 0.2% of the advective flux. We examined the vertical transport and resultant mixing of ^{137}Cs due to ASCs in relation to the vertical advective ^{137}Cs flux, which consists of several components. The total vertical advective ^{137}Cs flux (TCF) can be decomposed into the mean ^{137}Cs flux (MCF) and eddy ^{137}Cs flux (ECF) using a low-pass Butterworth frequency filter as:

$$TCF = Cw \approx \overline{C}\,\overline{w} + \overline{C'w'} \equiv MCF + ECF, \tag{5}$$

where C is the concentration of dissolved ^{137}Cs from SGF-L2, and w is the vertical velocity from ROMS-L2. The covariance term between the eddy and mean components almost vanishes and thus it can be assumed zero. To quantify the vertical transport by ASCs, the ECF is decomposed further into the mesoscale (m) and submesoscale (s) components, using the 2-D Gaussian filter described in section 4.1, as:

$$ECF = \overline{C'w'} \approx \overline{C'_m w'_m} + \overline{C'_s w'_s} \equiv ECF_m + ECF_s. \tag{6}$$

We first evaluated the rate of the ^{137}Cs inventory (viz., the total amount of ^{137}Cs) attributable to downward fluxes against that derived from the FNPP1 as the sum of the oceanic direct release and atmospheric deposition over the SGF-L2 domain. In other words, this rate is the amount of ^{137}Cs transported vertically past the prescribed depth (d_c) during a month (or between 13 March and 30 June) divided by the total amount of ^{137}Cs released from 13 March to 30 June. To obtain the subsurface ^{137}Cs inventory in Bq, we integrated the downward flux in Bq m^{-2} s^{-1} at a certain depth, d_c, over the SGF-L2 domain and the 4 month period between 13 March and 30 June 2011. The result is summarized in Figure 13 for the inventories beneath four different d_c values: (a) at the MLD (ranging between 10 and 80 m on average; Figure 10e), (b) $d_c = 100$ m, (c) 200 m, and (d) 300 m. Figure 13a shows that approximately 50% of the FNPP1-derived ^{137}Cs

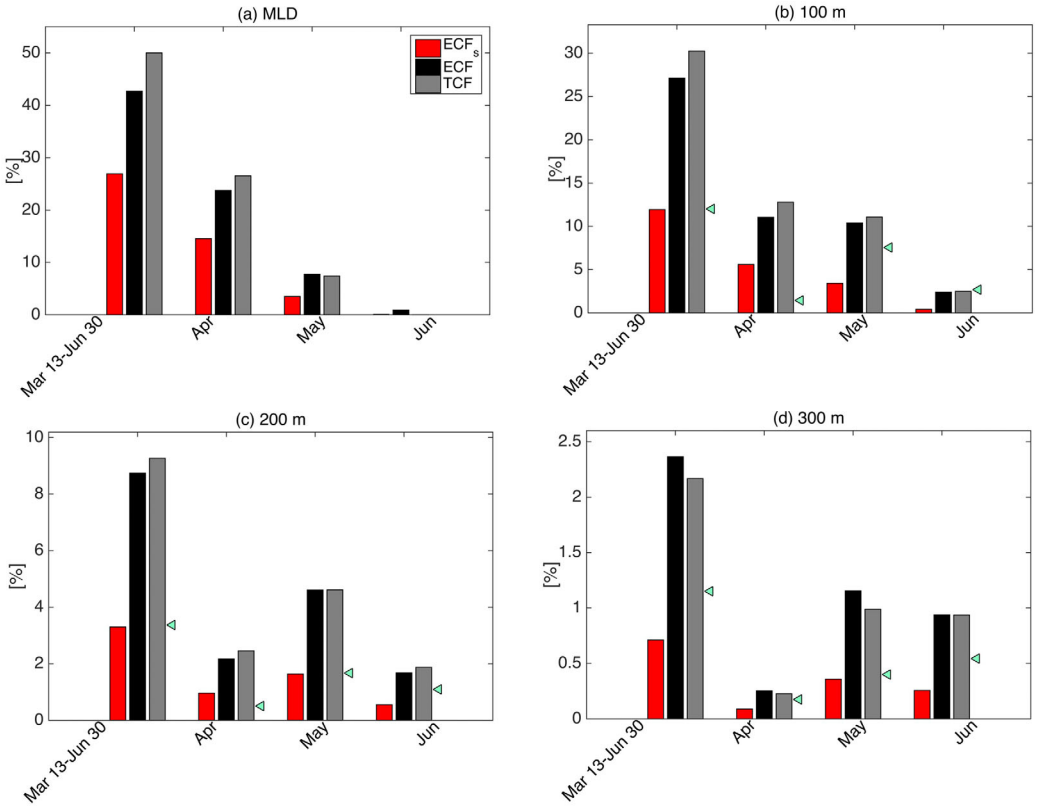

Figure 13. Ratios of the ^{137}Cs inventory in the SGF-L2 domain against the total ^{137}Cs load from oceanic direct release and atmospheric deposition. Inventories are estimated from the SGF-L2 model as the time-integrated and area-integrated downward vertical advective fluxes of the total ^{137}Cs flux (TCF, gray), eddy flux (ECF, black), and submesoscale eddy flux (ECFs, red). Area integrals are performed at four different depths, d_c, where (a) d_c is at the mixed-layer depth (MLD), (b) $d_c = 100$ m, (c) $d_c = 200$ m, and (d) $d_c = 300$ m. Cyan triangles in Figures 13b–13d are the corresponding TCF estimates from the SGF-M model. Note that in Figure 13d, TCF $<$ ECF because upward MCF occurs in deeper areas.

sank below the mixed layer, based on the TCF during the 4 month period. The contribution of the ECF was 42.7%, while that of the ECF$_s$ was 26.5%. Hence, the contribution of the submesoscale ECF$_s$ is quite substantial, reaching about 62% of the ECF and dominating over the mesoscale ECF$_m$. The maximum release rates and maximum inventory of ^{137}Cs also appear in April (Figures 2 and 10e), which has the most intensified submesoscale variability (section 4.2). Because of the coincidence of the most intensified submesoscale variability and the highest near-surface ^{137}Cs in April, the ECF$_s$ carried 14.5% of the total input below the mixed layer in April. This amount reduced over time to 3.5% in May and to 0.1% in June.

Figures 13b–13d show that the ECF dominates over MCF in each plot, confirming the importance of eddy-induced vertical transport to the subsurface ^{137}Cs inventory (Figure 10d). The maximum TCF contribution in April appears for $d_c = 100$ m (Figure 13b); however, in May, it appears in the deeper inventories for $d_c = 200$ m (Figure 13c) and 300 m (Figure 13d). This is considered a consequence of a residual effect of the eddy-induced downward transport that introduces a prominent time lag of about 1 month in the vertical transport behind the increase of near-surface ^{137}Cs. This is because the downward w values associated with ASCs are decreased considerably below the mixed layer (e.g., Gula et al., 2014; McWilliams et al., 2015). Nevertheless, the contribution of the submesoscale ECF$_s$ is still notable because it accounts for $\sim$1/3 of the TCF below the depth of 300 m for the 4 month period (Figure 13d). As the approximate temporal scale range for SCSs is hours to days (e.g., McWilliams, 2016), the SGF models might underestimate the effects of SCSs and ASCs on the vertical ^{137}Cs flux because of the under-resolved temporal variability of the daily averaged input field (section 2.2). If SGF-L2 used velocities averaged over shorter periods or as instantaneous values, the effect of submesoscale ECF$_s$ on vertical transport would appear more intense. However, this is beyond the scope of the present study and sampling frequencies of the input field will be examined elsewhere. On

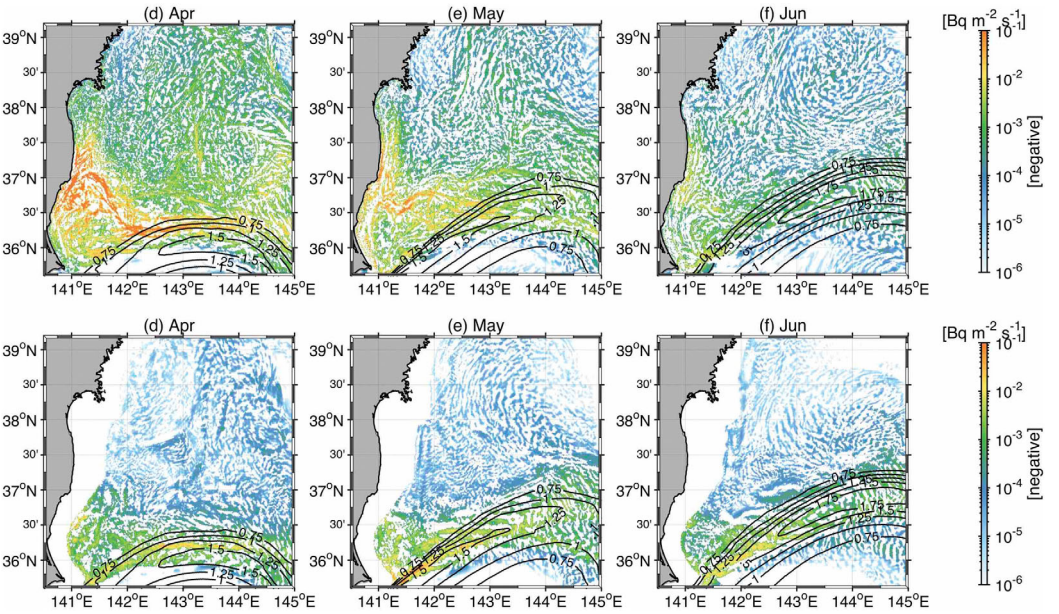

Figure 14. Spatial distribution of the monthly averaged submesoscale downward ^{137}Cs flux (ECF_s) for (a and d) April, (b and e) May, (c and f) June 2011. (top) ECF_s at the mixed-layer depth (MLD). (bottom) At $z = -200$ m. Black contours represent monthly averaged surface velocity magnitude at intervals of 0.25 m s^{-1}. Upward fluxes are blanked out.

the other hand, the cyan triangles in Figures 13b–13d represent the corresponding TCF estimated from the SGF-M. In general, SGF-M underestimates the total downward ^{137}Cs transport by about 1/3–1/2 that of SGF-L2 for the 4 month period. This underestimation is gradually recovered for $d_c = 100$ m (Figure 13b), presumably because of the imposed background vertical eddy diffusivity, K_s, which compensates the eddy-induced vertical ^{137}Cs transport detectable in SFG-M.

Figure 14 shows the spatial distribution of the monthly averaged submesoscale downward ECF_s at the MLD (Figures 14a–14c) and those at $z = -200$ m (Figures 14d–14f) for the 3 months. Note, only the mean downward ECFs are shown here and the upward ECFs are blank. The downward ECF_s at the MLD is enhanced extensively on the continental shelf near the coast off the FNPP1 with meridional elongation to the pattern found between 36.3°N and 37.6°N in April. A high ECF_s tongue develops from the bend of the coastline at around 37°N, 141°E toward the Kuroshio Extension Jet, where the high ECF_s is maintained along the Kuroshio front. As ASCs diminish in May and June (*n.b.*, Figures 11d–11f and 12b), ECF_s is also suppressed. Consistent with Figure 13c, the ECF_s at $z = -200$ m (Figures 14d–14f), which is sufficiently below the MLD, prevails in May (*n.b.*, ratios of the ^{137}Cs inventory are 1.0% in April, 1.6% in May, and 0.6% in June). The ECF_s at $z = -200$ m occurs only offshore of the continental shelf, which is remote from the area of high concentration of ^{137}Cs (Figure 7). Because of the combination of the distance from the source and the retarded w below the mixed layer, the maximum ECFs at $z = -200$ m lags that at the MLD by about 1 month. The Kuroshio Extension Jet is found to be at the center of the area in which deep downward transport occurs.

6. Discussion and Summary

We conducted a detailed hindcast of oceanic 3-D dispersal and initial dilution of dissolved ^{137}Cs, released from the FNPP1 accident, using a double-nested ROMS model embedded within an assimilative oceanic reanalysis (MOVE-WNP), coupled with an offline Eulerian ^{137}Cs transport model (the SGF model). The coupled SGF-L2 model had 1 km horizontal grid resolution, which was sufficient to represent SCSs and associated ASCs. A corresponding coarse-resolution model, SGF-M, was configured with a 10 km horizontal grid resolution, which enabled us to perform comparative assessments of the effects of SCSs on dispersal and dilution. We carried out extensive model-data comparisons against satellite altimetry data and field observations to demonstrate that both the SGF-L2 and SGF-M models could satisfactorily reproduce the Kuroshio, 3-D oceanic structure, and ^{137}Cs concentrations.

We exhibited that submesoscale dynamics are essentially important to better representation of the eddy field and the resultant ^{137}Cs transport. The submesoscale eddy-resolving SGF-L2 outperformed the coarse-resolution SGF-M, producing better agreement with the 3-D patterns of ^{137}Cs and an equivalent temporal variability of the surface ^{137}Cs near the FNPP1. For the initial dilution of the released ^{137}Cs, the SGF-M overestimated the cross-shelf transport, which led to unrealistically prompt entrainment of ^{137}Cs by the Kuroshio, whereas SGF-L2 manifested greater coastal trapping, alongshelf elongation, and temporal persistence in the near-surface ^{137}Cs distribution. In addition to the improvement in the lateral structure, SGF-L2 was able to represent the intensified vertical mixing and transport of ^{137}Cs due to ASCs. According to our energy conversion analysis, these ASCs occur most intensively on the submesoscale at wavelengths of 10–20 km, primarily because of shear instability, with baroclinic instability as the secondary mechanism. The emergence of SCSs has prominent seasonality, in which submesoscale intensification occurs in colder months, which is consistent with previous studies (e.g., Sasaki et al., 2014). The EKE and resultant eddy-induced ^{137}Cs transport were found intensified most in the coldest month (April 2011) during the study period, which corresponds to the period immediately after the FNPP1 accident.

To investigate the submesoscale influences on the vertical transport of ^{137}Cs, we introduced frequency and wave number filters for the decomposition into the mean (seasonal), mesoscale, and submesoscale components. During the first 4 month period following the accident, about 50% of the total input of the released ^{137}Cs within the study domain was transported downward below the mixed layer. Surprisingly, 84% of that was induced by eddies, with a contribution of 62% from submesoscale eddies. Far below the mixed layer, downward transport of ^{137}Cs occurred predominantly because of eddies. For instance, 8.8% (2.4%) of the total input was transported downward below $z = -200$ m (300 m) by eddies, with a submesoscale contribution of 3.2% (0.7%), which is still about 1/3–1/2 of the total eddy-induced ^{137}Cs flux. Although submesoscale ASCs barely reach such depths below the shallow mixed layer (e.g., Gula et al., 2014), residual effects might gradually transport ^{137}Cs vertically to depths >200 m. This is inferred from the increase of ^{137}Cs in deeper areas that is retarded by about 1–2 months in relation to the increase of surface ^{137}Cs.

Suppose if the FNPP1 accident were to occur in a much colder (warmer) season. Based on the outcomes of the present study, submesoscale eddies and SCSs would have been more (less) prominent. This could have caused immediate (retarded) subduction of high levels of ^{137}Cs into the deeper ocean, potentially provoking greater coastal contamination (immediate offshore dilution with possible entrainment by the Kuroshio) and thus, more significant regional (widespread) consequences. Furthermore, another important aspect can be deduced from the eddy-driven deep transport of ^{137}Cs that occurs at depth along the Kuroshio Extension. This process could lead to enhancement of the ^{137}Cs supply to subsurface waters (viz., Central Mode Water and Subtropical Mode Water), which subsequently transport ^{137}Cs via associated deep clockwise-circulating gyres on the southern side of the Kuroshio, returning the FNPP1-derived radionuclides to the western North Pacific margins in the long term. Indeed, such multiannual subsurface transport processes have already been detected (e.g., Kaeriyama et al., 2014; Kumamoto et al., 2017). We should also note that although the submesoscale eddy-resolving SGF-L2 produced the most satisfactory results without any substantial crude tuning of the model parameters, the coarse-resolution SGF-M has a central role in predicting an immediate first guess of the dispersal of radionuclides for much wider areas. However, this requires that an appropriate vertical eddy diffusivity K_s be determined a priori to account for seasonally varying submesoscale effects.

Acknowledgments

We are grateful to Norihisa Usui of MRI, JMA, for his technical support regarding the data input of MOVE-WNP. This study was supported by the Japan Society for the Promotion of Science grant-in-aid for Scientific Research (KAKENHI grants: 15H00977, 15H04049, and 15KK0207). The supporting information contains simulation data that enables the figures to be reproduced. The model output and computing codes used in this study are available from the authors upon request (kamidaira.yuki@jaea.go.jp). The oceanic release rate data of ^{137}Cs used in the oceanic dispersion simulation are available in the supporting information. The atmospheric release rate data of ^{137}Cs used in the oceanic dispersion simulation are available at https://www.atmos-chem-phys.net/15/1029/2015/acp-15-1029-2015-discussion.html. The MOVE-WNP product may be available at the Meteorological Research Institute upon a request. The SRTM30_Plus data are available at ftp://topex.ucsd.edu/pub/srtm30_plus/. The J-EGG500 data set is distributed by the JODC at http://jdoss1.jodc.go.jp/cgi-bin/1997/depth500_file. The MSLA (mapped sea-level anomaly) in delayed-time product was generated by Ssalto/Duacs and distributed by AVISO (ftp.aviso.altimetry.fr). The GPV-GSM/MSM atmospheric product was generated by the JMA and it is available from the repository at http://database.rish.kyoto-u.ac.jp/arch/jma-data/data/gpv/original/. The COADS data are maintained and distributed by NOAA at https://www.esrl.noaa.gov/psd/data/gridded/data.coads.1deg.

References

Aoyama, M., Hult, M., Hamajima, Y., Lutter, G., Marissens, G., Stroh, H., et al. (2016b). Tracing radioactivity from Fukushima in the Nnorthern Pacific Ocean. *Applied Radiation and Isotopes*, *109*, 435–440.

Aoyama, M., Kajino, M., Tanaka, T. Y., Sekiyama, T. T., Tsumune, D., Tsubono, T., et al. (2016a). ^{134}Cs and ^{137}Cs in the North Pacific Ocean derived from the March 2011 TEPCO Fukushima Dai-ichi Nuclear Power Plant accident, Japan. Part two: Estimation of ^{134}Cs and ^{137}Cs inventories in the North Pacific Ocean. *Journal of Oceanography*, *72*, 53–65.

Aoyama, M., Tsumune, D., Uematsu, M., Kondo, F., & Hamajima, Y. (2012). Temporal variation of ^{134}Cs and ^{137}Cs activities in surface water at stations along the coastline near the Fukushima Dai-ichi Nuclear Power Plant accident site. *Geochemical Journal*, *46*, 321–325.

Badin, G., Tandon, A., & Mahadevan, A. (2011). Lateral mixing in the pycnocline by baroclinic mixed-layer eddies. *Journal of Physical Oceanography*, *41*, 2080–2101.

Becker, J. J., Sandwell, D. T., Smith, W. H. F., Braud, J., Binder, B., Depner, J., et al. (2009). Global bathymetry and elevation data at 30 arcseconds resolution: SRTM30_PLUS. *Marine Geodesy*, *32*(4), 355–371.

Boccaletti, G., Ferrari, R., & Fox-Kemper, B. (2007). Mixed layer instabilities and restratification. *Journal of Physical Oceanography*, *37*, 2228–2250.

Buesseler, K. O., Dai, M., Aoyama, M., Benitez-Nelson, C., Charmasson, S., Higley, K., et al. (2017). Fukushima Daiichi-derived radionuclides in the ocean: Transport, fate, and impacts. *Annual Review of Marine Science*, *9*, 173–203.

Buesseler, K. O., Jayne, S. R., Fisher, N. S., Rypina, I. I., Baumann, H., Baumann, Z., et al. (2012). Fukushima-derived radionuclides in the ocean and biota off Japan. *Proceedings of the National Academy of Sciences of the United States of America*, *109*, 5984–5988.

Callies, J., Ferrari, R., Klymak, J. M., & Gula, J. (2015). Seasonality in submesoscale turbulence. *Nature Communications*, *6*, 6862. https://doi.org/10.1038/ncomms7862

Capet, X., McWilliams, J. C., Molemaker, J. M., & Shchepetkin, A. F. (2008a). Mesoscale to submesoscale transition in the California Current System. Part I: Flow structure, eddy flux, and observational tests. *Journal of Physical Oceanography*, *38*, 29–43.

Capet, X., McWilliams, J. C., Molemaker, J. M., & Shchepetkin, A. F. (2008b). Mesoscale to submesoscale transition in the California Current System. Part III: Energy Balance and Flux. *Journal of Physical Oceanography*, *38*, 2256–2269.

Dong, C., McWilliams, J. C., & Shchepetkin, A. F. (2007). Island wakes in deep water. *Journal of Physical Oceanography*, *37*, 962–981.

Estournel, C., Bosc, E., Bocquet, M., Ulses, C., Marsaleix, P., Winiarek, V., et al. (2012). Assessment of the amount of Cesium-137 released into the Pacific Ocean after the Fukushima accident and analysis of its dispersion in Japanese coastal waters. *Journal of Geophysical Research*, *117*, C11014. https://doi.org/10.1029/2012JC007933

Gula, J., Molemaker, M. J., & McWilliams, J. C. (2014). Submesoscale cold filaments in the Gulf Stream. *Journal of Physical Oceanography*, *44*, 2617–2643.

Inomata, Y., Aoyama, M., Tsubono, T., Tsumune, D., & Hirose, K. (2016). Spatial and temporal distributions of ^{134}Cs and ^{137}Cs derived from the TEPCO Fukushima Daiichi nuclear power plant accident in the North Pacific Ocean by using optimal interpolation analysis. *Environmental Science: Processes & Impacts*, *18*, 126–136.

Isoguchi, O., Shimada, M., & Kawamura, H. (2010). Characteristics of ocean surface winds in the lee of an isolated island observed by synthetic aperture radar. *Monthly Weather Review*, *139*, 1744–1761.

Kaeriyama, H., Shimizu, Y., Ambe, D., Masujima, M., Shigenobu, Y., Fujimoto, K., et al. (2014). Southwest intrusion of ^{134}Cs and ^{137}Cs derived from the Fukushima Dai-ichi Nuclear Power Plant accident in the Western North Pacific. *Environmental Science & Technology*, *48*, 3120–3127.

Kaeriyama, H., Shimizu, Y., Setou, T., Kumamoto, Y., Okazaki, M., Ambe, D., et al. (2016). Intrusion of Fukushima-derived radiocaesium into subsurface water due to formation of mode waters in the North Pacific. *Sci. Rep.*, *6*, 22010. https://doi.org/10.1038/srep22010

Kamidaira, Y., Uchiyama, Y., & Mitarai, S. (2017). Eddy-induced transport of the Kuroshio warm water around the Ryukyu Islands in the East China Sea. *Continental Shelf Research*, *143*, 206–218.

Katata, G., Chino, M., Kobayashi, T., Terada, H., Ota, M., Nagai, H., et al. (2015). Detailed source term estimation of the atmospheric release for the Fukushima Daiichi Nuclear Power Station accident by coupling simulations of atmospheric dispersion model with improved deposition scheme and oceanic dispersion model. *Atmospheric Chemistry and Physics*, *15*, 1029–1070.

Kawamura, H., Kobayashi, T., Furuno, A., In, T., Ishikawa, Y., Nakayama, T., et al. (2011). Preliminary numerical experiments on oceanic dispersion of 131I and ^{137}Cs discharged into the ocean because of the Fukushima Daiichi Nuclear Power Plant Disaster. *Journal of Nuclear Science and Technology*, *48*, 1349–1356.

Kawamura, H., Kobayashi, T., Furuno, A., Usui, N., & Kamachi, M. (2014). Numerical simulation on the long-term variation of radioactive cesium concentration in the North Pacific due to the Fukushima disaster. *Journal of Environmental Radioactivity*, *136*, 64–75.

Klein, P., Hua, B.-L., Lapeyre, G., Capet, X., Le Gentil, S., & Sasaki, H. (2008). Upper ocean turbulence from high-resolution 3D simulations. *Journal of Physical Oceanography*, *38*, 1748–1763.

Kubota, M., Nakata, K., & Nakamura, Y. (1981). Continental shelf waves off the Fukushima coast. Part I: Observations. *Journal of the Oceanographic Society of Japan*, *37*, 267–278.

Kumamoto, Y., Aoyama, M., Hamajima, Y., Nagai, H., Yamagata, T., Kawai, Y., et al. (2017). Fukushima-derived radiocesium in the western North Pacific in 2014. *Journal of Radioanalytical and Nuclear Chemistry*, *311*, 1209–1217.

Kunze, E., Klymak, J. M., Lien, R. C., Ferrari, R., Lee, C. M., Sundermeyer, M. A., et al. (2015). Submesoscale water mass spectra in the Sargasso Sea. *Journal of Physical Oceanography*, *45*, 1325–1338.

Large, W. G., McWilliams, J. C., & Doney, S. C. (1994). Oceanic vertical mixing: A review and model with a nonlocal boundary layer parameterization. *Reviews of Geophysics*, *32*, 363–403.

Le Traon, P. Y., Nadal, F., & Ducet, N. (1998). An improved mapping method of multisatellite altimeter data. *Journal of Atmospheric and Oceanic Technology*, *15*, 522–534.

Lévy, M., Klein, P., & Treguier, A.-M. (2001). Impact of submesoscale physics on production and subduction of phytoplankton in an oligotrophic regime. *Journal of Marine Research*, *59*, 535–565.

Mahadevan, A., & Archer, D. (2000). Modeling the impact of fronts and mesoscale circulation on the nutrient supply and biogeochemistry of the upper ocean. *Journal of Geophysical Research*, *105*, 1209–1225.

Mahadevan, A., & Tandon, A. (2006). An analysis of mechanisms for submesoscale vertical motion at ocean fronts. *Ocean Modelling*, *14*, 241–256.

Marchesiello, P., McWilliams, J. C., & Shchepetkin, A. (2003). Equilibrium structure and dynamics of the California Current System. *Journal of Physical Oceanography*, *33*, 753–783.

Marsaleix, P., Auclair, F., & Estournel, C. (2009). Low-order pressure gradient schemes in sigma coordinate models: The seamount test revisited. *Ocean Modelling*, *30*, 169–177.

Marsaleix, P., Auclair, F., Estournel, C., Nguyen, C., & Ulses, C. (2012). Alternatives to the Robert-Asselin filter. *Ocean Modelling*, *41*, 53–66.

Mason, E., Molemaker, J., Shchepetkin, A. F., Colas, F., McWilliams, J. C., & Sangrà, P. (2010). Procedures for offline grid nesting in regional ocean models. *Ocean Modelling*, *35*, 1–15.

Masumoto, Y., Miyazawa, Y., Tsumune, D., Tsubono, T., Kobayashi, T., Kawamura, H., et al. (2012). Oceanic dispersion simulations of ^{137}Cs released from the Fukushima Daiichi Nuclear Power Plant. *Elements*, *8*, 207–212.

McWilliams, J. C. (2016). Submeoscale currents in the ocean. *Proceedings of the Royal Society of London A*, *472*, 20160117. https://doi.org/10.1098/rspa.2016.0117

McWilliams, J. C., Gula, J., Molemaker, J., Renault, L., & Shchepetkin, A. F. (2015). Filament frontogenesis by boundary layer turbulence. *Journal of Physical Oceanography*, *45*, 1988–2005.

Miyazawa, Y., Masumoto, Y., Sergey, M., Varlamov, S. M., & Miyama, T. (2012). Transport simulation of the radionuclide from the shelf to open ocean around Fukushima. *Continental Shelf Research*, *50–51*, 16–29.

Miyazawa, Y., Zhang, R., Guo, X., Tamura, H., Ambe, D., Lee, J., et al. (2009). Water mass variability in the western North Pacific detected in 15-year eddy-resolving ocean reanalysis. *Journal of Oceanography*, *65*, 737–756.

Mori, N., Takahashi, T., Yasuda, T., & Yanagisawa, H. (2011). Survey of 2011 Tohoku earthquake tsunami inundation and run-up. *Geophysical Research Letters*, *38*, L00G14. https://doi.org/10.1029/2011GL049210

Nagai, T., Tandon, A., & Rudnick, D. L. (2006). Two-dimensional ageostrophic secondary circulation at ocean fronts due to vertical mixing and large-scale deformation. *Journal of Geophysical Research*, *111*, C09038. https://doi.org/10.1029/2005JC002964

Nagai, T., Tandon, A., Yamazaki, H., Doubell, M. J., & Gallager, S. (2012). Direct observations of microscale turbulence and thermohaline structure in the Kuroshio Front. *Journal of Geophysical Research*, *117*, C08013. https://doi.org/10.1029/2011JC007228

Nuclear Emergency Response Headquarters, Government of Japan (2011). *Report of Japanese government to the IAEA ministerial conference on nuclear safety—The accident at TEPCO's Fukushima Nuclear Power Stations—VI, Discharge of radioactive materials to the environment*. Retrieved from http://japan.kantei.go.jp/kan/topics/201106/iaea_houkokusho_e.html

Pérez, F. F., Gilcoto, M., & Ríos, A. F. (2003). Large and mesoscale variability of the water masses and the deep chlorophyll maximum in the Azores Front. *Journal of Geophysical Research*, *108*(C7), 3215. https://doi.org/10.1029/2000JC000360

Pollard, R. T., & Regier, L. A. (1992). Vorticity and vertical circulation at an ocean front. *Journal of Physical Oceanography*, *22*, 609–625.

Qiu, B. (2001). Kuroshio and Oyashio currents. In J. Steele, S. Thorpe, & K. Turekian (Eds.), *Encyclopedia of ocean sciences* (pp. 1413–1425). New York, NY: Academic Press.

Roads, J. (2004). Experimental weekly to seasonal U.S. forecasts with the regional spectral model. *Bulletin of the American Meteorological Society*, *85*, 1887–1902.

Rodriguez, E., Morris, C. S., Belz, J. E., Chapin, E. C., Martin, J. M., Daffer, W., et al. (2005). *An assessment of the SRTM topographic products* (Tech. Rep. JPL DO31639, 143 p). Pasadena, CA: Jet Propulsion Laboratory.

Romero, L., Uchiyama, Y., Ohlman, J. C., McWilliams, J. C., & Siegel, D. A. (2013). Simulations of nearshore particle-pair dispersion in Southern California. *Journal of Physical Oceanography*, *443*, 1862–1879.

Sasaki, H., Klein, P., Qiu, B., & Sasai, Y. (2014). Impact of oceanic-scale interactions on the seasonal modulation of ocean dynamics by the atmosphere. *Nature Communications*, *5*, 5636. https://doi.org/10.1038/ncomms6636

Shchepetkin, A. F., & McWilliams, J. C. (2005). The regional ocean modeling system (ROMS): A split-explicit, free-surface, topography-following-coordinate oceanic model. *Ocean Modelling*, *9*, 347–404.

Shchepetkin, A. F., & McWilliams, J. C. (2008). Computational kernel algorithms for fine-scale, multiprocess, longtime oceanic simulations. In R. Temam & J. Tribbia (Eds.), *Handbook of numerical analysis: Computational methods for the ocean and the atmosphere* (pp. 119–181). Amsterdam, the Netherlands: Elsevier.

Terada, H., & Chino, M. (2008). Development of an atmospheric dispersion model for accidental discharge of radionuclides with the function of simultaneous prediction for multiple domains and its evaluation by application to the Chernobyl nuclear accident. *Journal of Nuclear Science and Technology*, *45*, 920–931.

Thomas, L. N., & Taylor, J. R. (2010). Reduction of the usable wind-work on the general circulation by forced symmetric instability. *Geophysical Research Letters*, *37*, L18606. https://doi.org/10.1029/2010GL044680

Tsubono, T., Misumi, K., Tsumune, D., Bryan, F. O., Hirose, K., & Aoyama, M. (2016). Evaluation of radioactive cesium impact from atmospheric deposition and direct release fluxes into the North Pacific from the Fukushima Daiichi nuclear power plant. *Deep Sea Research, Part I*, *115*, 10–21.

Tsujino, H., Motoi, T., Ishikawa, I., Hirabata, M., Nakano, H., Yamanaka, G., et al. (2010). *Reference manual for the Meteorological Research Institute Community Ocean Model (MRI.COM) Version 3* (Tech. Rep. MRI 59). Tsukuba, Japan: Meteorological Research Institute.

Tsumune, D., Tsubono, T., Aoyama, M., & Hirose, K. (2012). Distribution of oceanic ^{137}Cs from the Fukushima Dai-ichi Nuclear Power Plant simulated numerically by a regional ocean model. *Journal of Environmental Radioactivity*, *111*, 100–108.

Tsumune, D., Tsubono, T., Aoyama, M., Uematsu, M., Misumi, K., Maeda, Y., et al. (2013). One-year, regional-scale simulation of ^{137}Cs radioactivity in the ocean following the Fukushima Dai-ichi Nuclear Power Plant accident. *Biogeosciences*, *10*, 5601–5617.

Uchiyama, Y., Idica, E. Y., McWilliams, J. C., & Stolzenbach, K. D. (2014). Wastewater effluent dispersal in Southern California Bays. *Continental Shelf Research*, *76*, 36–52.

Uchiyama, Y., Kanki, R., Takano, A., Yamazaki, H., & Miyazawa, Y. (2017b). Mesoscale reproducibility in regional ocean modeling with a 3-D stratification estimate based on Aviso-Argo data. *Atmosphere-Ocean*, *55*, 1–18.

Uchiyama, Y., Suzue, Y., & Yamazaki, H. (2017a). Eddy-driven nutrient transport and associated upper-ocean primary production along the Kuroshio. *Journal of Geophysical Research: Oceans*, *122*, 5046–5062. https://doi.org/10.1002/2017JC012847

Usui, N., Ishizaki, S., Fujii, Tsujino, Y. H., Yasuda, T., & Kamachi, M. (2006). Meteorological Research Institute multivariate ocean variational estimation (MOVE) system: Some early results. *Advances in Space Research*, *37*, 806–822.

Wilmott, C. J. (1981). On the validation of models. *Physical Geography*, *2*, 184–194.

Woodruff, S. D., Slutz, R. J., Jenne, R. L., & Steurer, P. M. (1987). A comprehensive ocean-atmosphere data set. *Bulletin of the American Meteorological Society*, *68*, 1239–1250.

Wright, D. G., Thompson, K. R., & Lu, Y. (2006). Assimilating long-term hydrographic information into an eddy-permitting model of the North Atlantic. *Journal of Geophysical Research*, *111*, C09022. https://doi.org/10.1029/2005JC003200